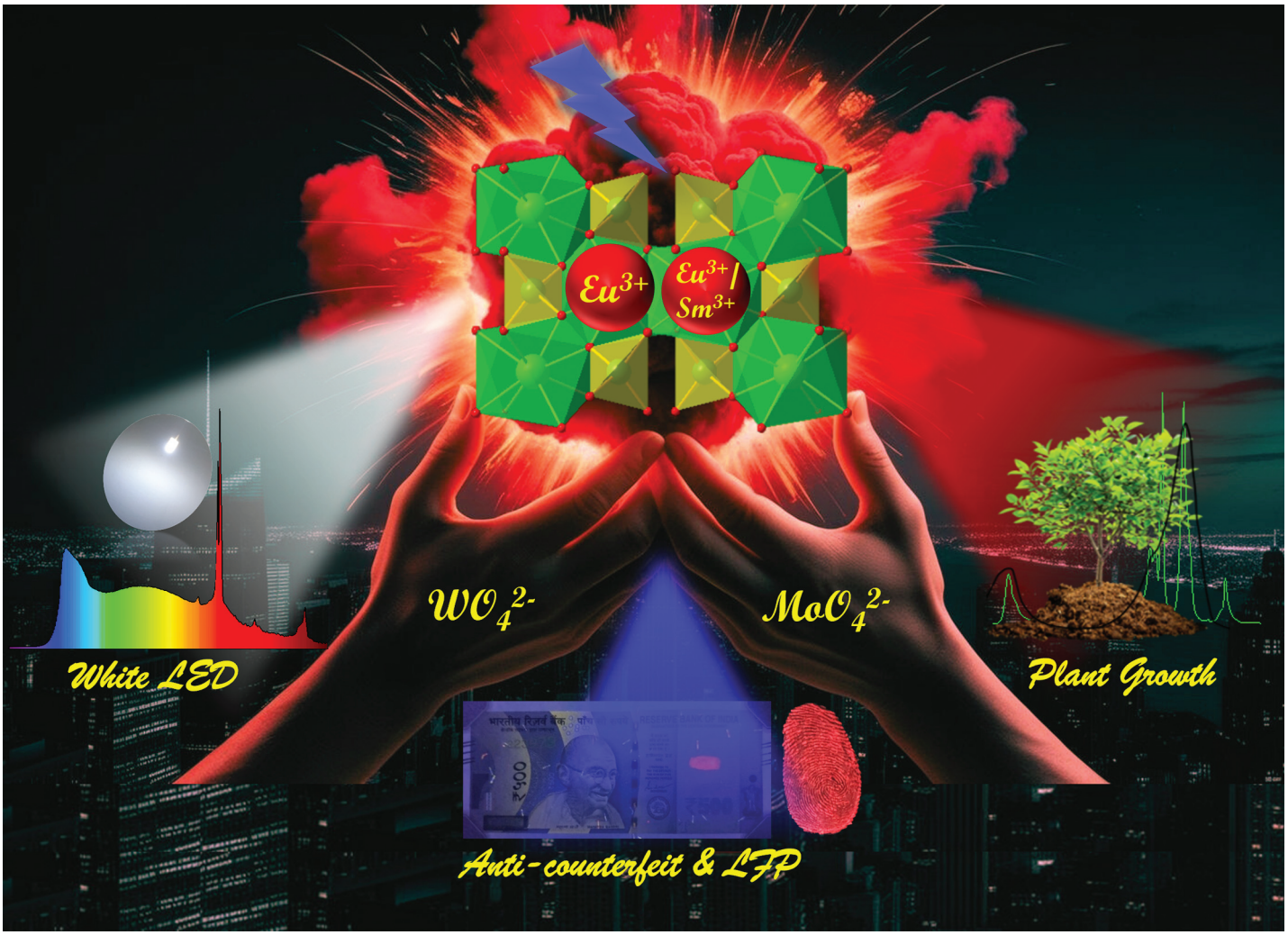

Showcasing research from Professor Sivakumar Vaidyanathan's laboratory, Department of Chemistry, Indian Institute of Technology Hyderabad, Sangareddy, Hyderabad, India.

Highly efficient red/orange-red emitting Eu^{3+} and Sm^{3+}/Eu^{3+} co-doped phosphors with their versatile applications

Highly emissive red phosphors were discovered and used for generating efficient white LEDs (CRI = 86 and CCT = 5371 K) and security applications (to identify latent fingerprints in the anti-counterfeiting field).

Image reproduced by permission of Sivakumar Vaidyanathan from *Dalton Trans.*, 2025, **54**, 6060.

As featured in:

See Priyadarshini Pradhan and Sivakumar Vaidyanathan, *Dalton Trans.*, 2025, **54**, 6060.

ROYAL SOCIETY OF CHEMISTRY

rsc.li/dalton

Registered charity number: 207890

Dalton Transactions

ROYAL SOCIETY OF CHEMISTRY

PAPER

View Article Online
View Journal | View Issue

Cite this: *Dalton Trans.*, 2025, **54**, 6060

Highly efficient red/orange-red emitting Eu^{3+} and Sm^{3+}/Eu^{3+} co-doped phosphors with their versatile applications†

Priyadarshini Pradhan[a] and Sivakumar Vaidyanathan *[b]

In the present work, a series of narrowband, red-emitting $Li_2La_4(MoO_4)_7:Eu^{3+}$ (LLM:Eu) phosphors were synthesized through a high-temperature conventional solid-state approach. All the synthesized phosphors crystallized in a tetragonal structure with the $I4_1/a$ space group. Either 395 nm near-UV light or 465 nm blue light can efficiently excite these synthesized phosphors, producing red light with a prominent wavelength of 616 nm. The optimum product of high-concentration quenching was $Li_2La_4(MoO_4)_7$:1.8Eu^{3+}, which reached a high color purity (CP) of 97.28% with a greater internal quantum efficiency (IQE) of 89.6%. The Eu^{3+} emission from the $Li_2La_4(MoO_4)_7$:1.8Eu^{3+} phosphor presents excellent thermal stability (81.75% at 423 K) demonstrated by temperature-dependent photoluminescence spectra. Solid solution phosphors were synthesized to enhance the photophysical properties in line with those mentioned above. The IQE and thermal stability were increased to 92.54% and 86.12%, respectively. When mixed with a yellow organic dye and a blue LED chip, our red component boosts the CRI and CCT of the customizable white light emitting diodes (WLEDs). The WLED produced using the $Li_2La_4(MoO_4)_7$:1.8Eu^{3+} red phosphor exhibited superior white light emission with good CRI (83) and CCT value (4925 K), which further improved (CRI = 86 and CCT = 5371 K) in the case of the $Li_2La_{2.2}Eu_{1.8}(MoO_4)_4(WO_4)_3$ solid solution phosphor. Prospective uses of the phosphors that are now being synthesized include security applications (to identify latent fingerprints and in the anti-counterfeiting field). Additionally, Eu^{3+}/Sm^{3+} co-doped red/deep red-emitting phosphors were synthesized and their photophysical properties were studied in detail to use them in the fabrication of red/deep-red LEDs as a light source to promote plant development.

Received 1st January 2025,
Accepted 16th February 2025

DOI: 10.1039/d5dt00004a

rsc.li/dalton

Introduction

Rare earth (RE) ion doped luminous materials have received substantial attention because they can be employed in a range of applications, including solid-state lighting (SSL), fiber amplifiers, plant growth, latent fingerprint, anti-counterfeiting, medical diagnosis, and optical sensors.[1–7] Phosphor-converted white light emitting diodes (pc-WLEDs), the third generation of lighting sources based on ultraviolet/blue LEDs, particularly benefit from the rising awareness of environmental protection and energy conservation. As a result of their various advantages, such as long lifetime, high rendering index, high luminous efficacy, ecological pollution reduction, low power consumption, and even the ability to save 50% of worldwide electricity, LEDs are considered an excellent replacement for incandescent and fluorescent bulbs.[8,9] The most popular method for producing white light emission relies on combining blue InGaN LED chips with Ce^{3+} doped garnet phosphors (YAG:Ce^{3+}).[10] Nevertheless, because the spectral dispersion in the red region is insufficient, the white light produced by this approach is inappropriate for general lighting and illumination, which raises the correlated color temperature (CCT) and lowers the color rendering index (CRI).[11] Red-emitting phosphors can be efficiently added to the system to fix the flaw. Therefore, finding appropriate red phosphors is crucial for producing efficient WLEDs. As a red phosphor for white LEDs, sulfides, nitrides, oxy-sulfides, and oxy-nitrides have all been developed thus far. Nonetheless, the hosts mentioned above have severe stability and synthetic condition issues.[12] To overcome these, many oxide-based red-emitting phosphors were synthesized and their optical properties were examined. The red phosphors obtained from oxide-based host lattices are simple to synthesize and have excellent thermal and chemical stability. Several nitride/oxy-nitride based Eu^{2+} activated red-emitting phosphors were reported, such as $CaAlSiN_3:Eu^{2+}$[13]

[a]*Department of Chemistry, National Institute of Technology, Rourkela, Odisha – 769008, India*
[b]*Department of Chemistry, Indian Institute of Technology, Hyderabad, Sangareddy, Kandi, Telengana – 502285, India. E-mail: vsiva@chy.iith.ac.in*

† Electronic supplementary information (ESI) available. See DOI: https://doi.org/10.1039/d5dt00004a

and $MSi_2O_2N_2$:Eu^{2+} (M = Ca, Sr, Ba).[14] This type of phosphor has a high quantum yield (QY) and good temperature resistance, but reabsorption of the blue and green components occurred. In addition, difficult synthesis conditions were required for these phosphors, resulting in high expenses. Moreover, the metal–N bonds in the nitride phosphors are more covalent than the metal–O bonds present in the oxide-based phosphors as a result of nitrogen's higher polarizability, smaller electronegativity and larger formal charge, which ultimately decreases the energy level (5d) of the activator ion Eu^{2+}. As a result, a significant portion of the nitride phosphors lies above 650 nm, which is invisible to the human eye, and the luminous efficacy will be reduced by such a high fraction of the emission band at long wavelengths.[15] Fluoride host based Mn^{4+} activated red emitting phosphors such as K_2TiF_6:Mn^{4+} (ref. 16) are suitable red phosphors for WLEDs because they can be excited by blue light and can produce several narrow red emissions in the range of 595–655 nm. However, the use of these phosphors is constrained by their poor thermal stability, hygroscopicity, and preparation-related environmental pollution issues.[17] To overcome the issues mentioned earlier, trivalent europium (Eu^{3+}) ions are studied for the preparation of red-emitting phosphors due to their ability to produce intense red emission around 616 nm as a result of the electric dipole transition ($^5D_0 \rightarrow {}^7F_2$).[18] Additionally, compared to the Eu^{2+}-activated red phosphors, producing Eu^{3+}-activated red phosphors under the air atmosphere is simpler and cheaper.

Additionally, indoor plant growth is another important application area for red/deep-red phosphors. Light is a plant's primary energy source and plays a significant role in plant development and growth through photosynthesis.[19,20] It is important to note that plants absorb light very selectively, and their growth is affected differently by distinct light sources depending on wavelength. It is well known that blue light with a wavelength of 450–480 nm improves photosynthesis, red light with a wavelength of 660–690 nm can enhance plant phototropism, and far-red light with a wavelength of 730–740 nm supports photomorphogenesis.[21] Plants have several photopigments; phytochrome photopigments (P_R and P_{FR}, which are interconvertible) play a crucial role in plant growth, and are particularly sensitive to red and far-red light.[22,23] LED lights should be able to span the absorption spectrum of phytochrome P_R, which plays a significant role in plants' growth process. Thus, LEDs, which can emit in the red/deep-red region by using red phosphors, are essential in the growth process of plants. In this regard, several reports on deep-red LEDs for indoor plant growth applications, including $LaMg_{0.5}(SnGe)_{0.5}O_3$:$Cr^{3+}$,[24] $CaY_{0.5}Ta_{0.5}O_3$:Mn^{4+},[25] and $ZnAl_2O_4$:Cr^{3+},[26] are available. However, the low absorption efficiency caused by the parity forbidden d–d transition of these luminous ions still limits the application of Mn^{4+} and Cr^{3+} activated far-red phosphors. Recently, numerous Eu^{3+} activated red/deep-red emitting phosphors have been studied for plant growth lighting LEDs, like $Ca_3Ga_2Ge_4O_{14}$:Eu^{3+},[27] $Ca_3Al_2Ge_3O_{12}$:Eu^{3+},[28] $LaAl_{0.7}Ga_{0.3}O_3$:Eu^{3+},Mn^{4+},[29] and $BaLaGaO_4$:Eu^{3+}.[30] These red phosphors have not covered the entire spectrum of phytochrome P_R absorption. Thus, the deep-red region needs to be covered by choosing appropriate red emitters. In the present work, efforts have been made to fabricate red/deep-red LEDs by taking Eu^{3+} and Sm^{3+} co-doped phosphors to cover the phytochrome P_R absorption spectrum completely. In addition, Eu^{3+} activated red emissive phosphors also have potential applicability in latent fingerprint (LFP) and anti-counterfeiting (AC).[31,32]

It is well known that Eu^{3+} exhibits weak optical absorption due to the forbidden nature of its electronic transitions. To enhance emission intensity or improve device efficiency, one potential strategy is to boost the activator ion concentration within the host lattice or move the charge transfer (CT) band more toward the blue or near-UV region (where the LED emission generally occurs). This can only be achieved by selecting suitable host lattices. Numerous oxide-based Eu^{3+} doped systems were reported, such as phosphates, borates, silicates, tungstates, and molybdates. The host materials often substantially influence the luminescence features of rare earth (RE) ions.[33,34] Therefore, the RE ions can exhibit the best luminous features by choosing an appropriate host material. In this regard, molybdates/tungstates have gained a great deal of attention presently because of their superior luminescence characteristics, deficient phonon energy, good chemical stability, and low synthesis temperature.[35,36] They make suitable host materials for red phosphors because W/Mo exhibits the most substantial charge transfer (CT) absorption in the UV range, the strongest covalent bond between W/Mo–O, the highest quenching concentration, and the greatest thermal stability. When exposed to NUV irradiation, the molybdate/tungstate host materials exhibit substantial absorption and transfer the absorbed energy to the activator ions, producing efficient color emission. Eu^{3+}-doped phosphor materials containing either MO_4 tetrahedra or MO_6 octahedra (M = W or Mo) are of great interest due to their high absorption in the near-ultraviolet to blue spectral range.[37] A novel double molybdate compound, $Li_2Gd_4(MoO_4)_7$, belongs to the tetragonal crystal system and was developed by Pandey *et al.* in the year 1974.[38] In 2012, $Li_2Tb_4(MoO_4)_7$ crystals were developed by Guo *et al.*[39] Later, Yu (2019) studied the Eu^{3+} activation for the $Li_2Gd_4(MoO_4)_7$ host lattice.[40] Under violet (396 nm) and blue (466 nm) light excitation, intense red fluorescence was revealed. In 2016, Ru *et al.*[41] synthesized Eu^{3+} activated $Li_2Y_4(MoO_4)_7$ red-emitting phosphors by the sol–gel method. Later, Zhao *et al.* (2021) studied the luminescence and energy transfer in $Li_2Y_4(MoO_4)_7$:Ln^{3+} (Ln = Dy, Eu) phosphors.[42] The synthesized samples showed tunable color emission from pale yellow to almost white in the CIE chromaticity coordinates by modifying the doping concentrations of Dy^{3+} and Eu^{3+} ions or shifting the excitation wavelength (353 nm to 391 nm). Recently, our group explored a few Eu^{3+}-activated red phosphors based on molybdate host lattices and studied their photophysical properties in detail. Impressive red emission with superior quantum yield was demonstrated using the $NaSrLa(MO_4)_3$:Eu^{3+} [M = Mo and W] red phosphor.[43] Rajendran *et al.* studied Eu^{3+} activation in $Na_2Ln_4(MoO_4)_7$ [Ln

= La, Gd, and Y] host lattices for hybrid white LEDs and plant growth applications.[44] So far, no research has been conducted on the Eu^{3+}-activated $Li_2La_4(MoO_4)_7$ host matrix.

In the present study, we reported a new and thermally stable red-emitting Eu^{3+}-activated $Li_2La_4(MoO_4)_7$ phosphor with high luminescence efficiency and color purity. Their phase purity, crystal structure, morphologies, luminescence properties, decay curves, thermal stability, and internal quantum efficiency (IQE) were thoroughly investigated. A series of solid solution phosphors between the tungstate and molybdate groups (WO_4^{2-} and MoO_4^{2-}) were synthesized with the optimized concentration of Eu^{3+} ions by a high-temperature solid-state approach to improve emission efficiency. Red and white LEDs were fabricated, and their electroluminescence (EL) properties were studied to investigate the potential application of synthesized phosphors. The synthesized high-efficiency red-emitting phosphors also impact the LFP and anti-counterfeiting applications. To further explore the phosphor's applicability for plant growth, Sm^{3+} and Eu^{3+} activated co-doped red phosphors were synthesized.

Experimental section

High-temperature solid-state reaction approach was executed for the synthesis of $Li_2La_{4-x}(MoO_4)_7{:}xEu^{3+}$ (x = 0–4 in the steps of 0.3), Sm^{3+}/Eu^{3+} co-doped, and solid solution phosphors. All the raw materials were of analytical grade and utilized without further processing. Li_2CO_3 (99%, Alfa Aesar), La_2O_3 (99.99%, Alfa Aesar), MoO_3 (ACS reagent ≥99.5%, Sigma-Aldrich), WO_3 (≥99%, Sigma-Aldrich), Eu_2O_3 (99.99% REO, Alfa Aesar), Sm_2O_3 (99.99% REO, Alfa Aesar), and Y_2O_3 (99.99% REO, Alfa Aesar) were utilized as the raw materials and weighed according to their stoichiometric ratio, properly mixed and ground with the help of an agate mortar. The samples were transferred to alumina crucibles and preheated in a muffle furnace at 600 °C for 10 h. After cooling to room temperature, the samples were further ground and sintered at 830 °C for 10 h. After cooling the furnace automatically to room temperature, a series of final products were obtained and collected in plastic vials after grinding for further characterization.

Results and discussion

Phase and structural analysis

Fig. 1a and S1† show the powder XRD patterns of the selected phosphor compositions, demonstrating that the diffraction peaks of the synthesized phosphors align well with the standard pattern (ICSD No. 66090). This confirms that the phosphors crystallized in a tetragonal structure belong to the space group of $I4_1/a$(88). The absence of any impurity peak in the diffraction pattern indicates the successful substitution of La^{3+} ions with incoming Eu^{3+} ions in the host lattice due to their similar ionic radii for coordination no. 8. As illustrated in Fig. 1b, the diffraction peaks of the phosphors exhibited a shift toward a higher 2θ angle with the rise in Eu^{3+} concentration, which is attributed to the incorporation of Eu^{3+}

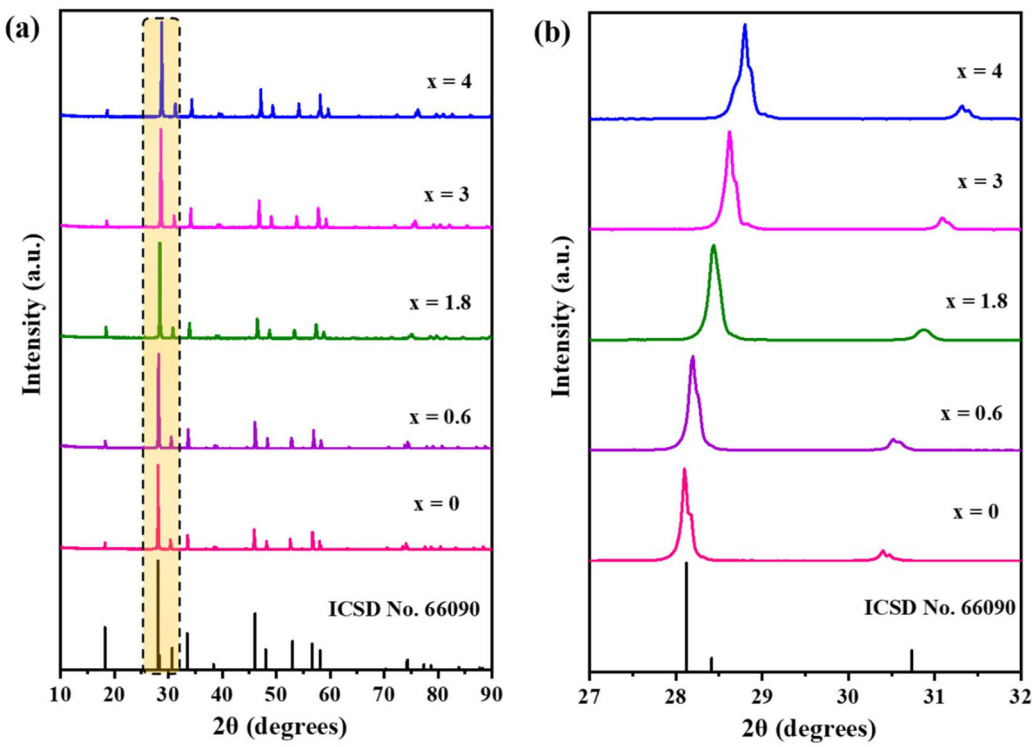

Fig. 1 (a) PXRD pattern of selected phosphor compositions of $Li_2La_{4-x}(MoO_4)_7{:}xEu^{3+}$ phosphors. (b) Enlarged XRD pattern with 2θ from 27 to 32°.

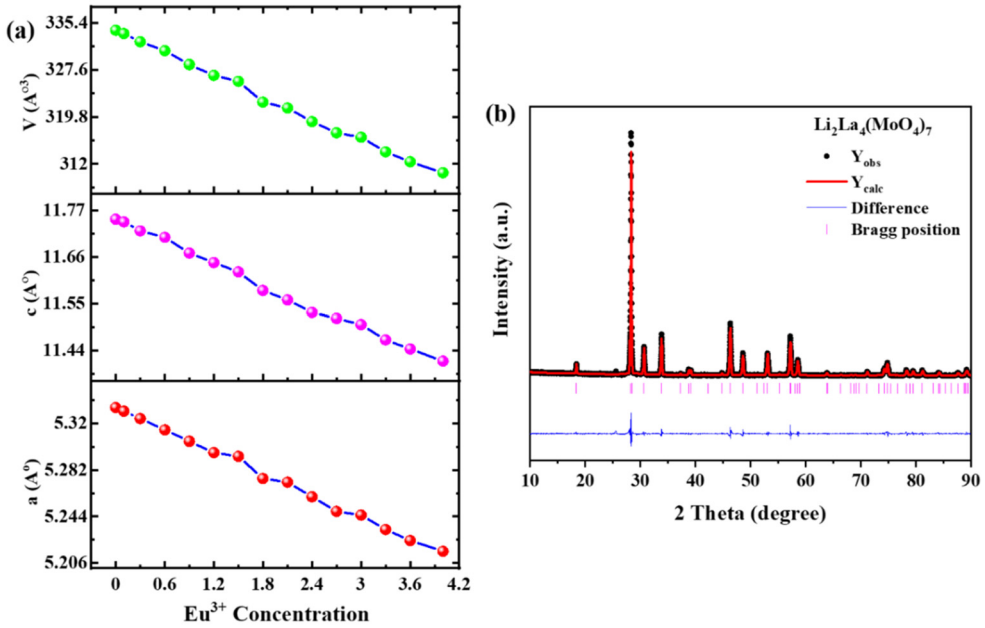

Fig. 2 (a) Lattice parameters of $Li_2La_{4-x}(MoO_4)_7$:xEu^{3+} phosphors and (b) Rietveld refinement of $Li_2La_4(MoO_4)_7$.

(1.066 Å) having smaller ionic radii in place of La^{3+} with slightly greater ionic radii (1.16 Å). To further validate the crystal structure, Rietveld refinement was conducted on $Li_2La_4(MoO_4)_7$ (Fig. 2b). Since no structural study of $Li_2La_4(MoO_4)_7$ has been previously documented, and no reference file exists in international databases (such as crystallographic online databases, ICSD or COD), we had to rely on the crystal data for $NaLa(WO_4)_2$ (ICSD code: 66090), which shows a similar scheelite structure. The refined parameters are summarized in Table 1 with low R factor values, and the atomic coordinates are presented in Table ST1.† In the $Li_2La_4(MoO_4)_7$ host lattice, all the lattice parameter values continuously decreased with the rise in Eu^{3+} ion concentration, as seen in Fig. 2a and summarized in Table ST2.†

The crystal structure of the $Li_2La_4(MoO_4)_7$ phosphor is illustrated in Fig. 3a, which resembles the scheelite structure of $CaMoO_4$.[45] In the crystal structure, the Li^+ and La^{3+} ions occupy the same site and are coordinated with eight oxygen atoms, with bond lengths ranging from 2.285 to 2.502 Å

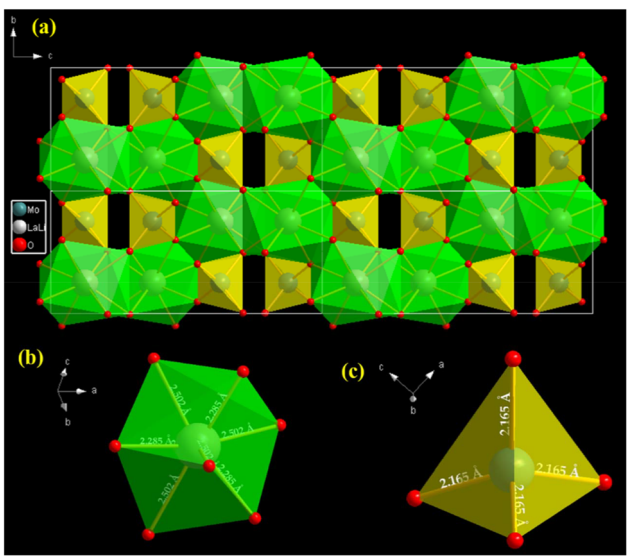

Fig. 3 (a) Crystal structure of $Li_2La_4(MoO_4)_7$, coordination environment and bond lengths of (b) Li/La and (c) Mo, respectively.

Table 1 Refinement parameters for LLM phosphors

Compound	$Li_2La_4(MoO_4)_7$
Crystal system	Tetragonal
Space group	$I4_1/a$(88)
a & b (Å)	5.3306(1)
c (Å)	11.7490(2)
$\alpha = \beta = \gamma$	90°
V (Å^3)	334.1625(1)
Z	4
2θ-interval	10–90°
R_{wp}, %	10.87
R_p, %	8.42
GOF	1.86

(Fig. 3b). As shown in Fig. 3c, Mo is coordinated with four oxygen atoms to form the MoO_4 unit, with a Mo–O bond length of 2.165 Å.

Surface morphology study

Particle morphology, including factors such as size, shape, defects, size distribution, and other characteristics, is known to impact the luminous properties of the phosphor particles. The surface morphology of the host and Eu^{3+} activated phosphors was investigated using the SEM technique, and the

corresponding images are shown in Fig. S2.† The creation of the microcrystalline structure, as seen in the SEM micrographs, is attributed to the agglomeration of grains resulting from the sintering of the samples at high temperatures. The size of the particles is erratic, varying from 1 to 5 μm. Fig. S2† shows the elemental mapping and EDX spectra to examine the composition and element distribution of LLM:1.8Eu^{3+} phosphor. The presence of constituted elements of the phosphor sample is clearly visible from the elemental mapping and EDX spectrum except Li (because Li is not detectable due to too low X-ray energy).

Fourier-transform infrared (FT-IR) spectroscopy study

Fourier transform infrared spectroscopy (FT-IR) is a structural diagnostic tool for studying molecular vibrations. The FT-IR spectra of Eu^{3+} activated $Li_2La_4(MoO_4)_7$ is depicted in Fig. S3† in the 400–4000 cm^{-1} region. The molybdate stretching vibrations typically appear in the 600–940 cm^{-1} range. The symmetric stretching vibrations of the Mo–O bonds in the MoO_4 tetrahedra are responsible for the peak at 912 cm^{-1}. The broad band at 832 cm^{-1} and the peak at 710 cm^{-1} result from the asymmetric streching vibrations of the Mo–O bands in the distorted MoO_4 tetrahedra. The peak at 611 cm^{-1} can be attributed to the streching vibrations of the Mo–O–Mo bond. The asymmetric bending vibrations in the tetrahedra produce a strong peak at 411 cm^{-1}. The stretching vibrations of the MoO_4 group are often found below 500 cm^{-1}. The 400–500 cm^{-1} range may also have stretching vibrations from La–O and Eu–O bonds.[46,47]

Diffuse reflectance spectra and band gap analysis

Fig. 4a shows the UV diffuse reflectance spectra of the host LLM and some selected compositions of Eu^{3+} doped LLM phosphors. The broad absorption band (200–350 nm) was observed due to charge transfer from O^{2-} to Mo^{6+} and Eu^{3+} ions. A group of sharp peaks were observed by the Eu^{3+} doped phosphor in the range of 350–550 nm due to f–f electronic transitions. The Tauc plots produced from the absorption spectral data are shown in Fig. 4b, and by using the Kubelka–Munk equation,[48] the band gap values were determined:

$$F(R_\infty) = \frac{(1-R_\infty)^2}{2R_\infty} = \frac{K}{S} \quad (1)$$

Here, R_∞ is the ratio of the diffuse reflectance of the sample concerning the standard sample, while K and S stand for the absorption and scattering coefficients, respectively. The following Tauc–Wood relationship directly links the optical band gap (E_g) to the incident light's frequency (υ) and linear absorption coefficient:[49]

$$\alpha h\upsilon = A(h\upsilon - E_g)^n \quad (2)$$

The proportionality constant is denoted as A, $h\upsilon$ stands for the light energy, and n represents the electronic transition values as 1/2, 2, 3/2, and 3 for direct allowed, indirect allowed, direct forbidden, and indirect forbidden transition, respectively.[50] A thorough analysis of the $Li_2La_4(MoO_4)_7$ phosphors has shown that their transition is a direct allowed one. The Kubelka–Munk plot for the DRS spectra is illustrated in Fig. 4b, from which the E_g values were calculated (3.64 eV for the host and 3.58 eV for the LLM:1.8Eu^{3+} phosphor) by extrapolating the linear portion of the curve to the x-axis. As seen in Fig. 4b, the band gap decreased from 3.64 eV to 3.19 eV upon increasing Eu^{3+} concentration. This occurs due to the formation of defect energy levels introduced by Eu^{3+} ions within the band gap of the host lattice. These defect levels facilitate electron transfer from O^{2-} to intermediate Eu^{3+} orbitals, leading to a red shift in the band gap.[51]

Photoluminescence, asymmetric ratio, and concentration quenching study

The red-emitting phosphor's photoluminescence excitation (PLE) and emission (PL) spectra were examined. In the spectra

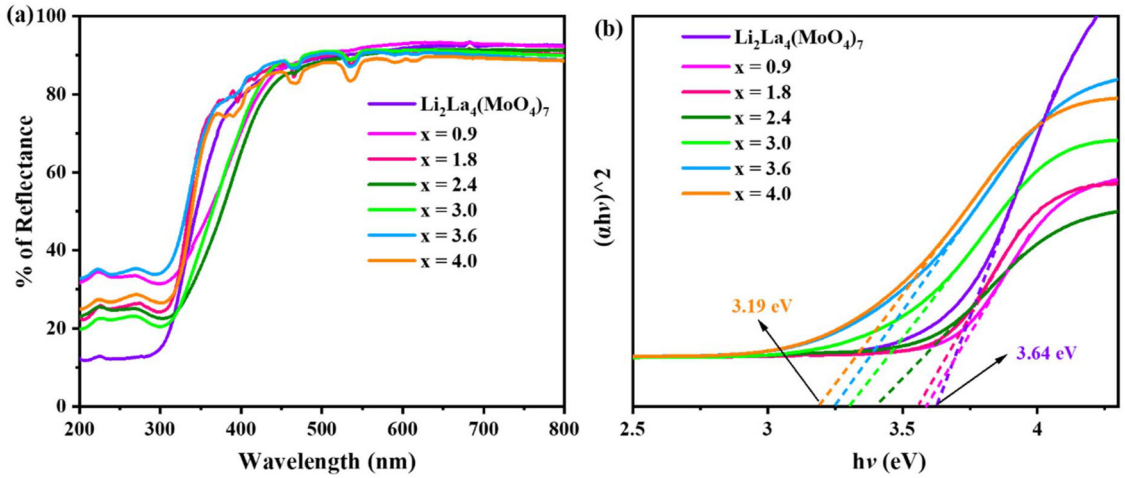

Fig. 4 (a) Diffuse reflectance spectra of the selected phosphor compositions of $Li_2La_{4-x}(MoO_4)_7$:xEu^{3+} and (b) band gap calculation using the Kubelka–Munk function.

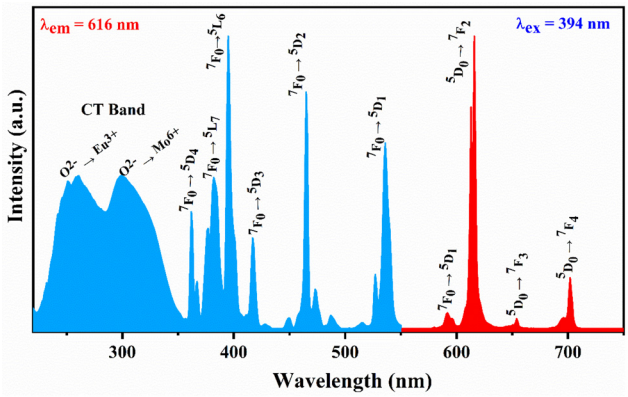

Fig. 5 Photoluminescence spectra of $Li_2La_4(MoO_4)_7$:1.8Eu^{3+}.

(Fig. 5), emission peaks corresponding to $^5D_0 \rightarrow {}^7F_J$ (J = 0–4) transitions with the dominating luminescence at 616 nm ($^5D_0 \rightarrow {}^7F_2$) appeared when the samples were excited at 395 nm. Fig. 6a illustrates the excitation spectra of $Li_2La_{4-x}(MoO_4)_7$:xEu^{3+} phosphors, recorded at the monitoring wavelength of 616 nm. A broad excitation band between 220 and 355 nm and a collection of sharp line-like peaks in the 356–550 nm range make up the excitation spectra of LLM:Eu^{3+} phosphors. $O^{2-} \rightarrow Eu^{3+}$ and $O^{2-} \rightarrow Mo^{6+}$ charge transfer bands (CTB), which are highly overlapping and indistinguishable, should be superimposed to form the broad excitation band ranging from 220 to 355 nm (with maxima at 260 and 300 nm). The f–f transitions of Eu^{3+} ions from the ground state ($^7F_0$) to the excited states ($^5D_4$, $^5L_7$, $^5L_6$, $^5D_3$, and $^5D_2$) are responsible for the sharp peaks at 362, 381, 395, 416, and 465 nm, respectively.[52] Notably, in the excitation spectra amid all the excitation peaks, the two most substantial peaks were situated at 395 and 465 nm, which are in good agreement with the emission wavelengths of near UV and blue LED chips, respectively. The emission spectra are depicted in Fig. 6b–d. Excitation of Eu^{3+} at 395 nm exhibited the strongest emission intensity among the excitation wavelengths, followed by 465 nm and the CT band, as shown in Fig. S4.† Four major characteristic peaks at 593, 616, 650, and 704 nm, corresponding to the transitions of the Eu^{3+} ion (*i.e.*, $^5D_0 \rightarrow {}^7F_1$, $^5D_0 \rightarrow {}^7F_2$, $^5D_0 \rightarrow {}^7F_3$, and $^5D_0 \rightarrow {}^7F_4$), were identified in the emission spectra.[53,54]

It can be seen from Fig. 5 that the $^5D_0 \rightarrow {}^7F_2$ transition (transition of electric dipole (ED)) at 616 nm exhibited a predominance of red emission, which is hypersensitive to the local crystal field environment. At 593 nm, the magnetic dipole (MD) transition causes the $^5D_0 \rightarrow {}^7F_1$ transition, independent of the host environment. The ED and MD transitions, which describe the local environment of the Eu^{3+} ion, are of great interest. Since the ED transition of Eu^{3+} is extremely sensitive, the crystal field environment significantly impacts the emission spectrum. According to Judd–Ofelt theory,[55] the red emis-

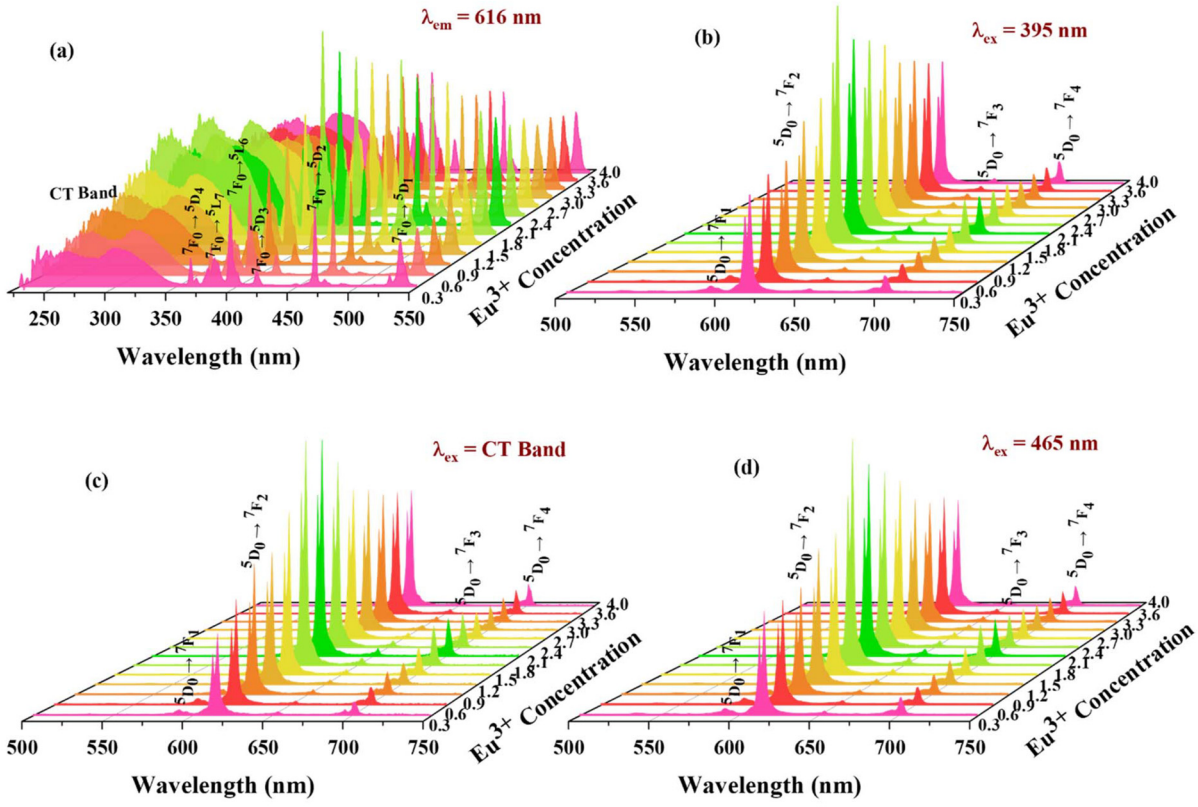

Fig. 6 PL (a) excitation and (b–d) emission spectra of $Li_2La_4(MoO_4)_7$ with variable concentration of Eu^{3+} ions.

sion (616 nm) from the imposed electric dipole (ED) transition ($^5D_0 \rightarrow {}^7F_2$) would typically predominate in the spectra when Eu^{3+} occupies the non-inversion center position in the lattice. On the other hand, when Eu^{3+} enters the inversion center, the yellow emission at 593 nm from the parity-allowed magnetic dipole (MD) transition ($^5D_0 \rightarrow {}^7F_1$) may predominate.[56] Surprisingly, the crystal field and local coordination have little effect on MD, although they significantly impact the ED. By comparing the relative intensities of the MD and ED transitions, it is possible to determine the local crystal symmetry of the host structure. In lanthanide-based systems, the I_{0-2}/I_{0-1} emission ratio (known as the asymmetric ratio (AR)) can therefore be utilized as a probe for a cation surrounding. Fig. 7b presents the plot of the I_{0-2}/I_{0-1} ratio against the Eu^{3+} ion concentration, with values ranging from 17.27 to 19.45. A higher AR indicates that the activator ions (Eu^{3+}) are in highly distorted crystal environments. The AR value gradually increased with rising Eu^{3+} ion concentration, reaching its peak at the optimal dopant concentration before decreasing. Since all the phosphors exhibited an AR greater than 1, the Eu^{3+} ions inhabited non-centrosymmetric sites, which are advantageous for achieving good color purity. The full width at half maximum (FWHM) and AR values for all synthesized Eu^{3+} activated phosphors were calculated (under the excitation at the CT band, 395 and 465 nm) and are presented in Table ST3.† Experimental results demonstrated that all samples exhibited narrow bright red emission with FWHM values < 5.5 nm. Red-emitting phosphors with narrow emission bands (FWHM < 30 nm) are known to significantly enhance the performance of white LEDs.

To find out the ideal doping concentration of Eu^{3+} ions in the $Li_2La_4(MoO_4)_7$ host lattice, emission spectra were recorded at various Eu^{3+} concentrations, as shown in Fig. 6b–d. All synthesized phosphors exhibited characteristic Eu^{3+} emissions when excited at 395 nm, but with varying relative intensities. The concentration of Eu^{3+} ion strongly affects the PL emission. A further finding from the concentration-dependent PL emission profile (Fig. 6b) was that, due to the concentration quenching effect, the PL emission intensity first showed an upward tendency with an increase in Eu^{3+} ion concentration before showing a decrement tendency with a further increase in dopant concentration. The resulting compounds exhibited the most vigorous PL emission intensity, reaching their maximum value when x was 1.8, indicating it as the ideal doping concentration of Eu^{3+} ions in the $Li_2La_4(MoO_4)_7$ host lattice. It is widely acknowledged that concentration quenching is a process that depends on distance, which occurs due to

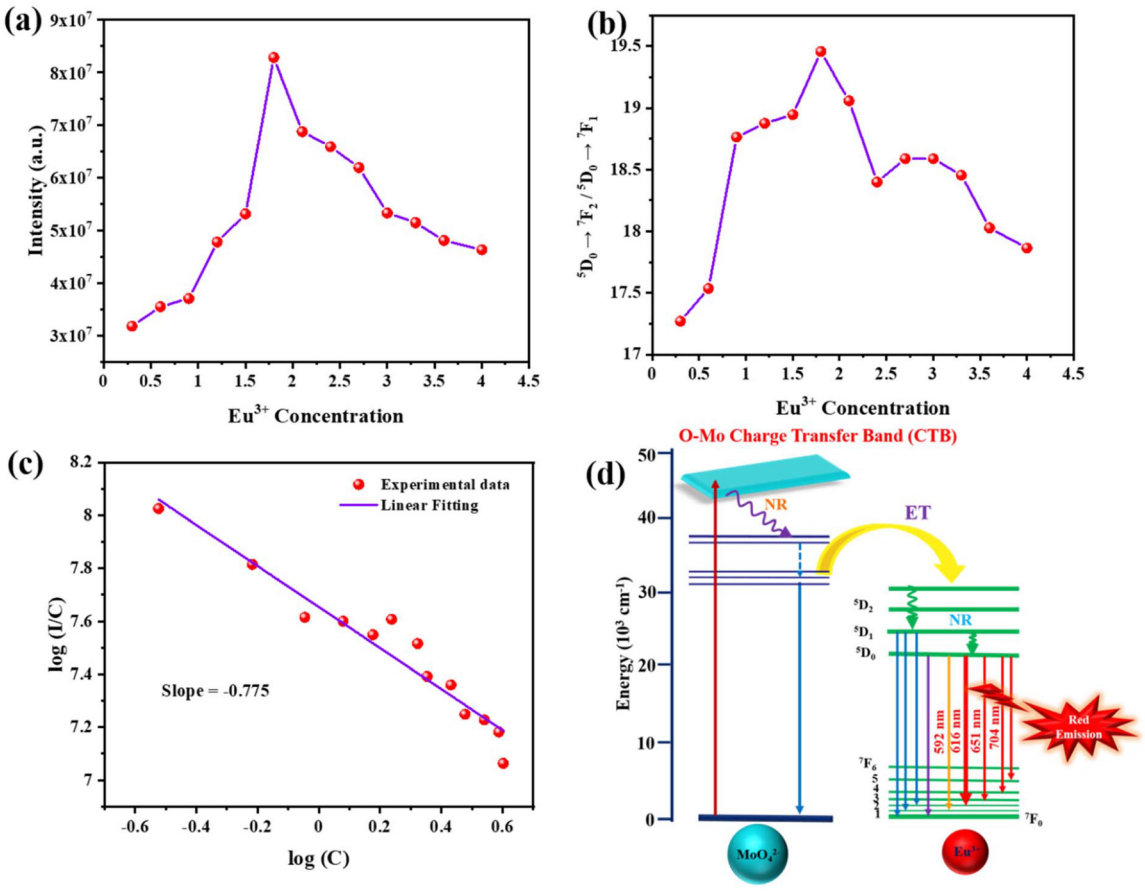

Fig. 7 (a) Eu^{3+} concentration *vs.* emission intensity of ED transition ($^5D_0 \rightarrow {}^7F_2$). (b) Asymmetric ratio of LLM:xEu^{3+} phosphors. (c) Linear relationship between log*C* and log(*I*/*C*). (d) Schematic representation of energy transfer to Eu^{3+} from the host in the lattice.

the energy transfer between neighbouring Eu^{3+} ions in the host lattice. As the Eu^{3+} doping concentration increases, the distance between Eu^{3+} ions decreases, enhancing interactions and facilitating non-radiative energy transfer, which ultimately reduces emission intensity.

Blasse's theory describes that the exchange or multipole–multipole interaction causes the non-radiative energy transfer. By determining the critical distance between the nearby Eu^{3+} ions, the kind of interaction can be identified, which is given by the Blasse equation:[57]

$$R_c = 2\left(\frac{3V}{4\pi X_c Z}\right)^{\frac{1}{3}} \quad (3)$$

where Z is the number of sites available for Eu^{3+} dopants to occupy per unit cell, and R_c, X_c, and V represent the critical distance, optimum concentration of the dopant ion, and critical cell volume, respectively. In this current investigation, the critical distance (X_c), volume (V), and Z of the unit cell are 1.8, 334.1625 Å^3, and 4, respectively. The critical distance was found to be 4.46 Å, nearly equal to 5 Å. The estimated R_c value shows that radiative transitions are preferred over non-radiative ones because of the strong energy transfer between adjacent activator ions.

Huang's hypothesis explains the type of interactions based on the relationship between activator concentration (C) and emission intensity (I).[58] The theory states that the subsequent eqn, (4) and (5), establish the relationship between I and C.

$$I = a^{\left(1-\frac{s}{d}\right)}\Gamma\left(1+\frac{s}{d}\right) \quad (4)$$

$$a = C\Gamma\left(1-\frac{d}{s}\right)\left[X_0\left(1+\frac{A}{\gamma}\right)\right]^{\frac{d}{s}} \quad (5)$$

In the above equation, X_0 and A are constants, the intrinsic transition probability of the sensitizer is represented as γ, Γ function is written as $\Gamma\left(1+\frac{s}{d}\right)$, and s stands for electric multipole index, which is 6, 8, and 10 for the electric dipole–dipole (D–D), dipole–quadrupole (D–Q), and quadrupole–quadrupole (Q–Q) interactions, respectively. This kind of interaction is considered an exchange when s is 3. The dimension of the sample is represented by d, and here it is 3. Eqn (4) and (5) can be rewritten as follows:

$$\log\frac{I}{C} = -\frac{s}{d}\log C + \log f \quad (6)$$

Here in this equation, the variables C and I represent the activator's concentration and emission intensity ($^5D_0 \rightarrow {}^7F_2$, ED transition), respectively, while f is a constant that remains constant regardless of the dopant concentration. To estimate the s value, $\log(C)$ and $\log(I/C)$ plotted together are shown in Fig. 7c. As can be seen from the graph, the experimental data fit linearly with a slope ($-s/d$) of approximately −0.775, close to 1. Consequently, the s value was 3, indicating that an exchange interaction mechanism was responsible for the energy transfer between activator ions in LLM:Eu^{3+} phosphors.

Enhanced emission intensity was exhibited by the solid solution phosphors in contrast to the parent phosphor. Replacing the MoO_4^{2-} group with the WO_4^{2-} group resulted in stronger and more pronounced absorption for both the CT band and 4f–4f transitions. By examining the strong red emission of the solid solution phosphors $Li_2La_{2.2}Eu_{1.8}(MoO_4)_{7-y}(WO_4)_y$ at 616 nm, excitation spectra were recorded at varying W^{6+} concentrations, as shown in Fig. 8a. The solid solution phosphors exhibited an excitation profile similar to that of the parent phosphor. Fig. 8b–d present the emission spectra of all solid solution phosphors obtained under excitation at the CT band, 395, and 465 nm. Like the parent phosphor, all the solid solution phosphors displayed the same emission profile. The 395 nm excited emission spectrum exhibited significantly higher intensity among the excitation wavelengths. The impact of W^{6+} can be seen in the emission profiles as a gradual increase in intensity, which was observed with the increasing W^{6+} ion content up to y = 3 (optimal doping concentration), and after that, it started decreasing. According to these PL results, adding W^{6+} ions to the existing phosphor is an intense way to improve its luminescence properties.

A solid solution between La^{3+} and Y^{3+} ions was also prepared by fixing the Eu^{3+} ion concentration at 1.8 and its PL properties were studied. However, no remarkable enhancement in the emission intensity was observed. At 395 and 465 nm excitation, a slight increase in emission intensity was observed when the Y^{3+} concentration was 0.2; however, it began to diminish thereafter. In contrast, under CT band excitation, the parent phosphor exhibited higher intensity (Fig. S5†).

Energy transfer mechanism

The schematic diagram of energy transfer from the MoO_4^{2-} group to the Eu^{3+} ion is depicted in Fig. 7d. The passage of the 2p electrons of O^{2-} to the 5d orbital of Mo^{6+} causes charge transfer bands (CTB) to form when the molybdate group is activated by absorbing UV radiation. Through the non-radiative relaxation process, electrons from the higher excited state of MoO_4 return to the ground level. In addition, part of its energy is transferred to the higher excited level of Eu^{3+} ion. Concurrently, the Eu^{3+} ions were excited from the $^7F_0$ to the $^5L_6$ level when the phosphors are excited at 395 nm. The electrons in higher excited states relaxed to the lowest excited $^5D_0$ through a non-radiative relaxation mechanism. The distinctive emissions of Eu^{3+} ions result from multiple radiative transitions from $^5D_0$ to ^7F_J (J = 1, 2, 3, 4) states, with peaks at 593, 616, 650, and 704 nm, respectively.[43]

Lifetime analysis

The luminescence decay curves of LLM:xEu^{3+} phosphors were obtained under 395 nm excitation, with the monitoring wavelength at 616 nm, as shown in Fig. 9a. All decay profiles were well fitted with a single exponential function. The experimental lifetime values for the $^5D_0 \rightarrow {}^7F_2$ transition of Eu^{3+} ions were determined utilizing the subsequent equation:[59]

$$I(t) = I_0 e^{-\frac{t}{\tau}} \quad (7)$$

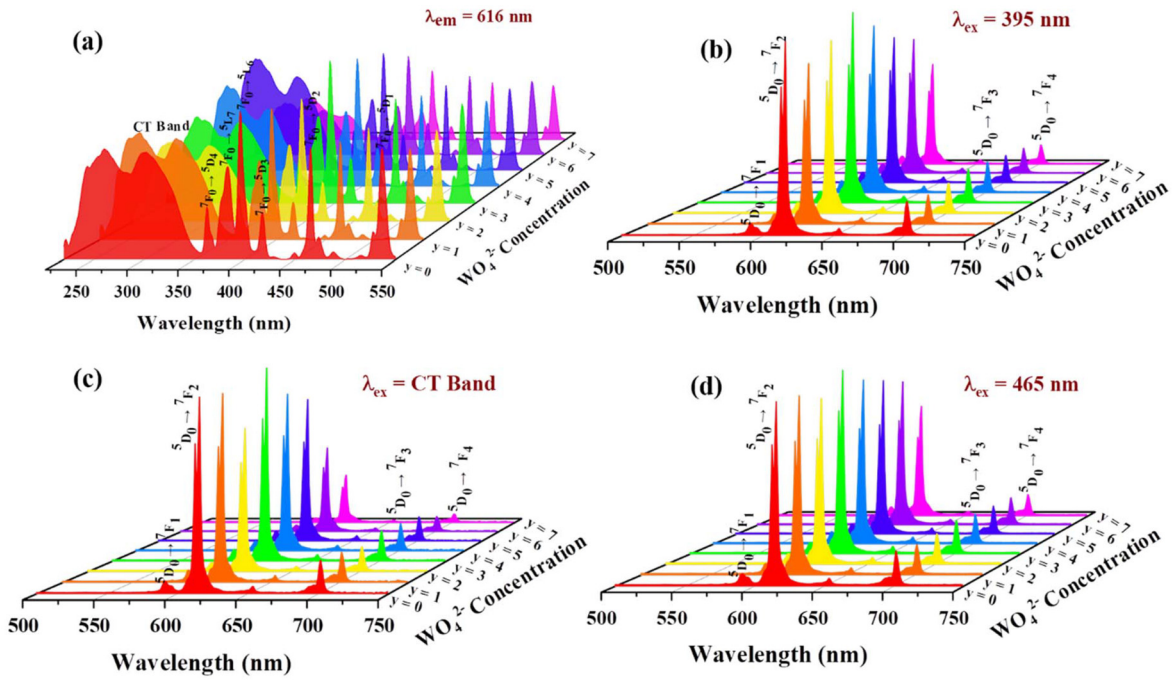

Fig. 8 PL (a) excitation and (b–d) emission spectra of solid solution phosphors $Li_2La_{2.2}Eu_{1.8}(MoO_4)_{7-y}(WO_4)_y$.

where the emission intensities at time t = 0 and t = t are denoted as I_0 and $I(t)$; t is the time, and τ represents the fluorescence lifetime. The calculated lifetime values are mentioned in Fig. 9b. From the decay curves and estimated values, it was observed that with the rise in Eu^{3+} concentration, initially, there is an increase in the lifetime values of Eu^{3+} activated LLM red-emitting phosphors until concentration quenching, after which gradual reduction in lifetime values was observed with a further rise in Eu^{3+} concentration. This occurs because increasing the Eu^{3+} ion concentration in the lattice reduces the distance between activator ions, enhancing energy transfer between neighbouring Eu^{3+} ions and leading to the induction of a non-radiative energy migration pathway.[60]

CIE color coordinates, color purity, and internal quantum efficiency

CIE chromaticity coordinates are a crucial factor to consider when assessing the luminous performance of phosphors. Using the relative PL spectra generated by excitation at 395 nm, the chromaticity coordinates for LLM:xEu^{3+} phosphors were calculated, and the obtained values are listed in Table ST4.† LLM:1.8Eu^{3+} showed chromaticity coordinates (0.6697, 0.3299) quite close to the NTSC standard red emission (0.670, 0.330). The CIE chromaticity coordinates of the LLM:1.8Eu^{3+} phosphor with the commercial red phosphor (Y_2O_2S, Y_2O_3) are shown in Fig. 10b. The samples' chromaticity

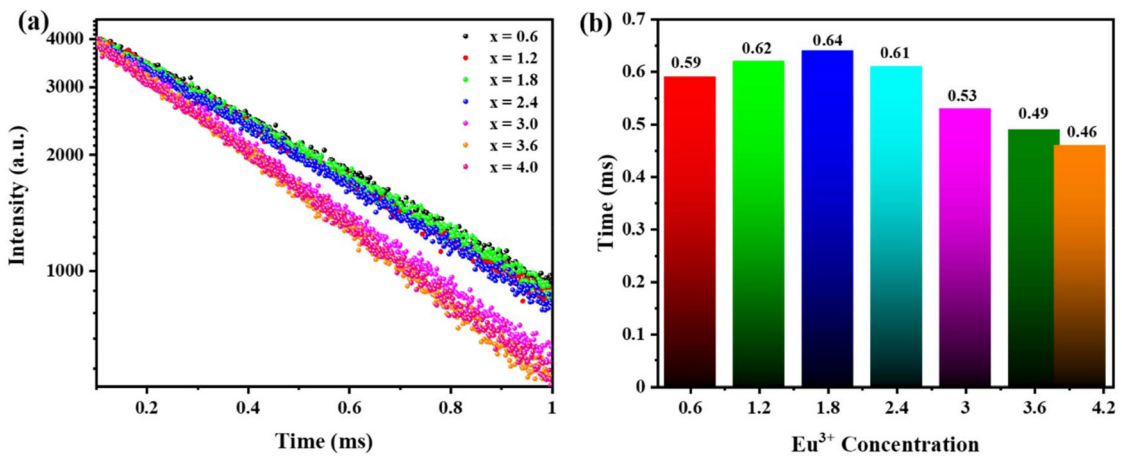

Fig. 9 (a) Decay curve analysis of $Li_2La_4(MoO_4)_7$:xEu^{3+} phosphors. (b) Calculated lifetime values.

coordinates are at the edge of the CIE 1931 chromaticity diagram, indicating that the LLM:xEu^{3+} phosphors have a high degree of color purity. A phosphor's color purity is a crucial factor in determining its chrominance properties, which can be done utilizing the following equation:[16]

$$\text{Color purity} = \frac{\sqrt{(x - x_i)^2 + (y - y_i)^2}}{\sqrt{(x_d - x_i)^2 + (y_d - y_i)^2}} \quad (8)$$

where (x, y) stands for the CIE chromaticity coordinates of the LLM:xEu^{3+} phosphors, (x_i, y_i) refers to as the white illuminant point, which is (0.333, 0.333), and (x_d, y_d) is known as the dominant wavelength point equal to (0.668, 0.335). The color purity of all the synthesized phosphors at different wavelengths was calculated and the results are listed in Tables ST4 and ST5.† Amid all the phosphors, LLM:1.8Eu^{3+} exhibited the highest color purity (λ_{ex} = 395 nm) as 97.28%, more significant than the color purity of previously reported Eu^{3+} activated red phosphors, such as KBaLu(MoO$_4$)$_3$:Eu^{3+},[61] KBaGd(MoO$_4$)$_3$:Eu^{3+},[62] and Na$_2$Gd(PO$_4$)(MoO$_4$):Eu^{3+}.[63] The LLM:Eu^{3+} phosphors can be used as the red components in warm white LEDs since they have excellent color purity and good CIE coordinates.

A comparison study of PL emission intensities was carried out between the synthesized (LLM:1.8Eu^{3+}) and commercially available red phosphors (Y$_2$O$_3$:Eu^{3+}, Y$_2$O$_2$S:Eu^{3+}) to demonstrate the possible use of our currently studied phosphors. At 395 nm excitation, the LLM:1.8Eu^{3+} phosphor exhibited an emission intensity 4.65 and 3.17 times higher than Y$_2$O$_2$S:Eu^{3+} and Y$_2$O$_3$:Eu^{3+}, respectively (Fig. 10a). Another crucial factor to consider when selecting a luminous material for numerous applications, particularly in pc-LEDs, is its efficiency. As shown in Fig. 10c, the internal quantum efficiency (IQE) of the sample LLM:1.8Eu^{3+} was calculated using the integrating sphere method at room temperature, with BaSO$_4$ as the reference. The IQE can be determined by utilizing the following equation:[64]

$$\eta = \frac{\int L_S}{\int E_R - \int E_S} \quad (9)$$

where IQE is represented as η, E_S and E_R stand for the excitation light in the presence and absence of the sample in the integrating sphere, and the emission spectrum of the currently studied phosphor is denoted as L_S. Under the excitation of 395 nm, the IQE of the as-synthesized phosphor LLM:1.8Eu^{3+} was determined to be 89.6%, which is higher than that of the commercially available phosphor Y$_2$O$_2$S:Eu^{3+} (35%) and some previously reported Eu^{3+} based red phosphors (Table ST6†). Yet, with the solid solution phosphor Li$_2$La$_{2.2}$Eu$_{1.8}$(MoO$_4$)$_4$(WO$_4$)$_3$, this IQE was improved and found

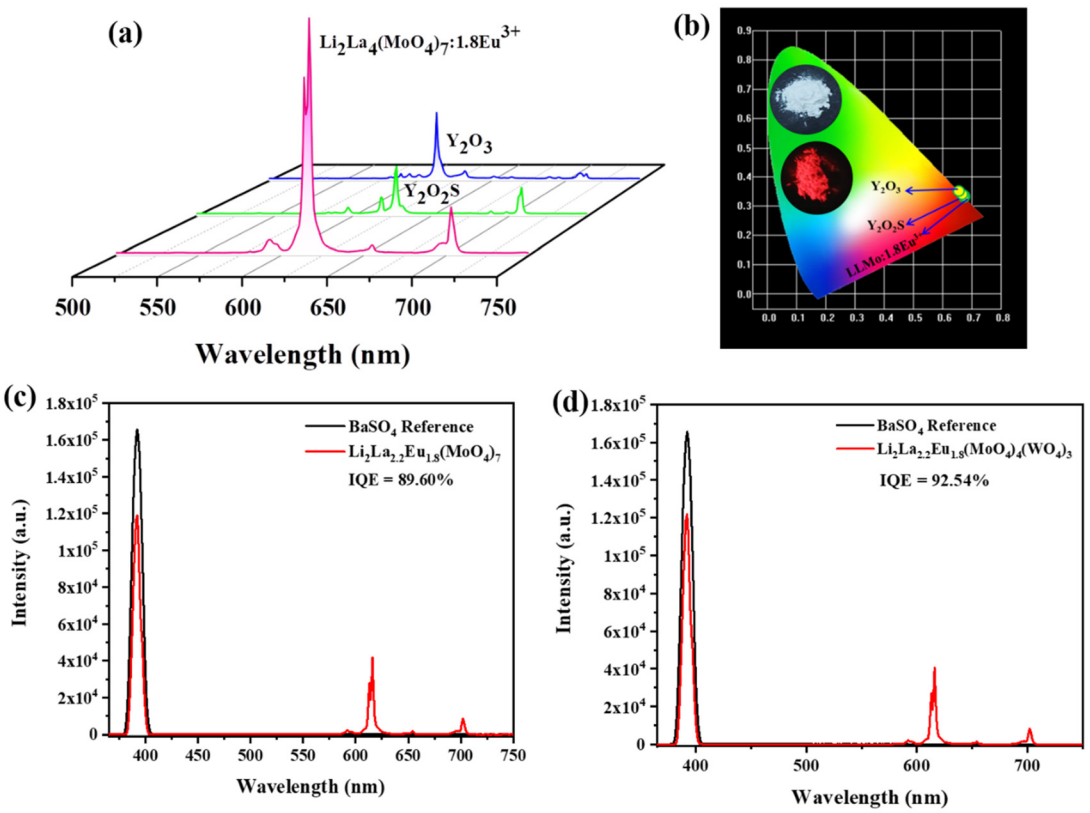

Fig. 10 (a) Comparative emission spectrum of LLM:1.8Eu^{3+} phosphor with commercial phosphors under the excitation at 395 nm. (b) CIE of LLM:1.8Eu^{3+}. Internal quantum efficiency (IQE) for (c) LLM:1.8Eu^{3+} and (d) Li$_2$La$_{2.2}$Eu$_{1.8}$(MoO$_4$)$_4$(WO$_4$)$_3$.

to be 92.54%. Additionally, the value of external quantum efficiency (EQE) can be computed with the help of the following formula:

$$\eta_{EQE} = \frac{\int L_S}{\int E_R} \quad (10)$$

As a result, the EQE of LLM:1.8Eu^{3+} was estimated to be 25.31%, and that for the solid solution phosphor ~24.46%. As a result of this occurrence, LLM:xEu^{3+} phosphors were shown to be suitable as a red-emitting component for SSL.

Thermal stability analysis

Because the surface temperature of an LED chip often reaches up to 150 °C during the work process, especially for high-power LED devices, it is acknowledged that the thermal stability of a phosphor is a significant technological characteristic for its practical uses.[65] The temperature-dependent PL study was carried out for the LLM:1.8Eu^{3+} phosphor in the temperature range of 25–200 °C, under the excitation of 395 nm (as shown in Fig. 11a) to explore the thermal quenching capability of the synthesized phosphors. A decline in the emission intensity was observed in the emission spectra with the rise in temperature due to the thermal quenching effect.[66] As the temperature rises, the thermally induced ionization process causes some excited electrons of Eu^{3+} ions to jump from the $^5D_0$ level into the O^{2-}–Eu^{3+} CTB, lowering the emission intensity.[61,67] The inset of Fig. 11a depicts the temperature dependence of emission intensity. It was discovered that the LLM:1.8Eu^{3+} phosphor retained 81.35% of its initial emission intensity at 423 K compared to that at room temperature. However, the thermal stability increased to 86.12% (Fig. 11c) in the case of the solid solution phosphor ($Li_2La_{2.2}Eu_{1.8}(MoO_4)_4(WO_4)_3$). To better comprehend the temperature dependency behavior of LLM:1.8Eu^{3+} and the solid solution phosphor, an Arrhenius fitting of their emission intensity with temperature is depicted in Fig. 11b and d. Additionally, the activation energy (E_a) for the thermal quenching process can be determined by the following Arrhenius equation:[68]

$$I_t = \frac{I_0}{1 + c\exp\left(\frac{-\Delta E_a}{kT}\right)} \quad (11)$$

In this equation, I_0 represents the initial emission intensity of the phosphor, and I_t is the emission intensity at various

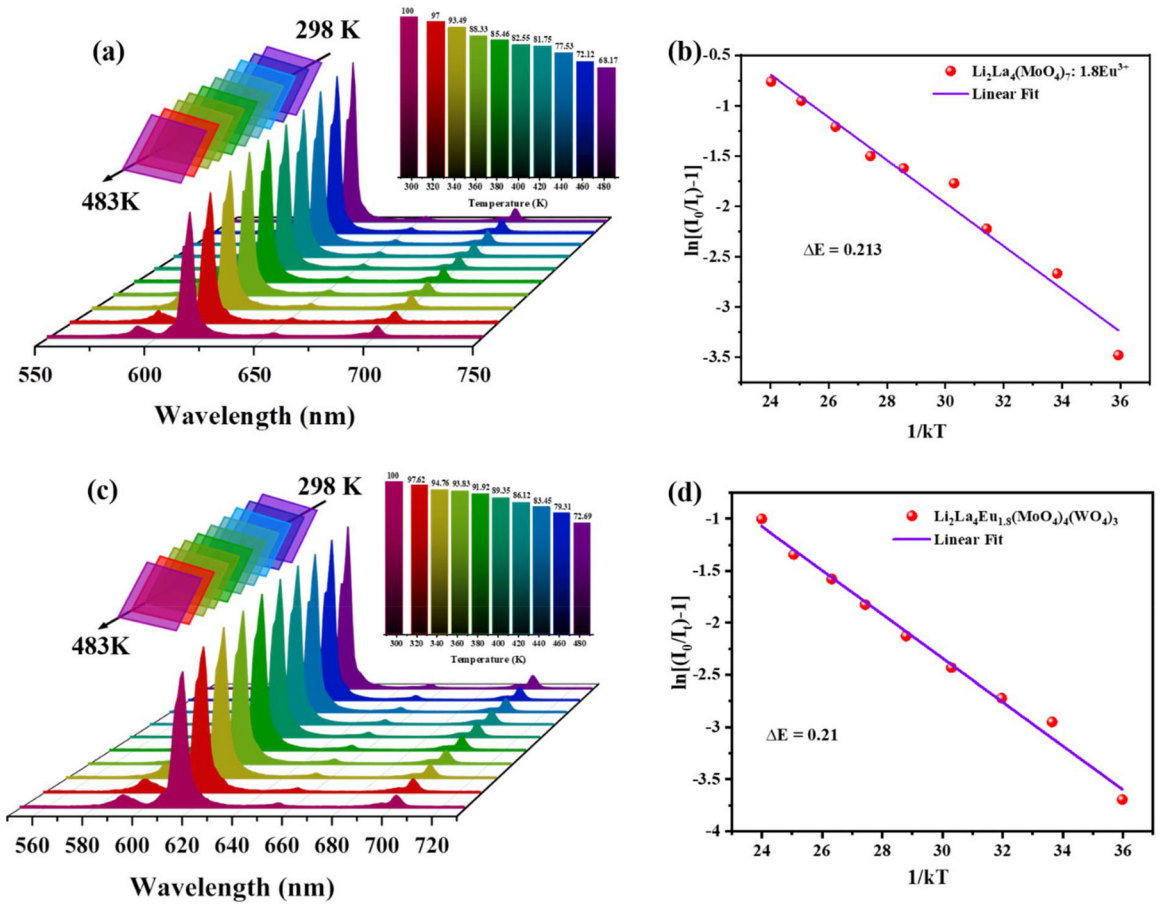

Fig. 11 Temperature dependent emission spectra (λ_{ex} = 395 nm), inset: normalized intensity variation with varying temperatures of (a) LLM:1.8Eu^{3+} and (c) $Li_2La_{2.2}Eu_{1.8}(MoO_4)_4(WO_4)_3$ solid solution phosphors. Plots of $\ln[(I_0/I) - 1]$ *vs.* $1/kT$ for (b) LLM:1.8Eu^{3+} and (d) $Li_2La_{2.2}Eu_{1.8}(MoO_4)_4(WO_4)_3$.

temperatures; activation energy is denoted as E_a, c is a constant for a particular host, and k is the Boltzmann constant (8.629×10^{-5} eV K^{-1}). Additionally, a logarithmic transfer can be used to make the aforementioned calculation more understandable.

$$\ln\left[\left(\frac{I_0}{I_t}\right) - 1\right] = \frac{-\Delta E_a}{kT} + \ln c \quad (12)$$

A linear relationship was observed between $\ln\left(\frac{I_0}{I_t} - 1\right)$ and $\frac{1}{kT}$ in the plot with a slope of −0.213 and −0.21 for LLM:1.8Eu^{3+} and $Li_2La_{2.2}Eu_{1.8}(MoO_4)_4(WO_4)_3$, respectively, as depicted in Fig. 11b and d. Consequently, E_a was found to be 0.213 and 0.21 eV for both the studied phosphors. These activation energies are significantly higher than some previously reported Eu^{3+}-based red phosphors (a comparison study is given in Table ST7†). The activation energy (E_a) is a representation of the thermal quenching energy barrier. Thermal stability improves with the increase in the E_a value. A low E_a value facilitates the activation of electrons from the $^5D_0$ level of Eu^{3+} to the O^{2-}–Eu^{3+} CTB upon temperature increase; however, this also results in a greater loss of excitation energy and a worsening of thermal quenching. Thus, its relatively high activation energy demonstrated the exceptional thermal stability of LLM:1.8Eu^{3+} and $Li_2La_{2.2}Eu_{1.8}(MoO_4)_4(WO_4)_3$ phospors. These results indicated the favourable thermal stability of the studied phosphors and might be a good choice for white LEDs.

Judd–Ofelt parameters

The Judd–Ofelt parameters, derived from the emission spectra that provide information about the non-radiative transition of the Eu^{3+} ions in the host lattice, are an excellent tool for understanding the spectrum characteristics of RE^{3+} ion intensity. The Judd–Ofelt theory calculations determine the optical intensity parameters (Ω_λ, λ = 2, 4, 6) to study the site symmetry and spectral characteristics of Eu^{3+} ions in the presently studied phosphors. The intensity parameters Ω_2 and Ω_4 were calculated for $^5D_0 \rightarrow {}^7F_2$ and $^5D_0 \rightarrow {}^7F_4$ transitions by fixing the $^5D_0 \rightarrow {}^7F_1$ transition as a reference according to the previous reports.[69,70] Even so, the intensity parameter Ω_6 is not

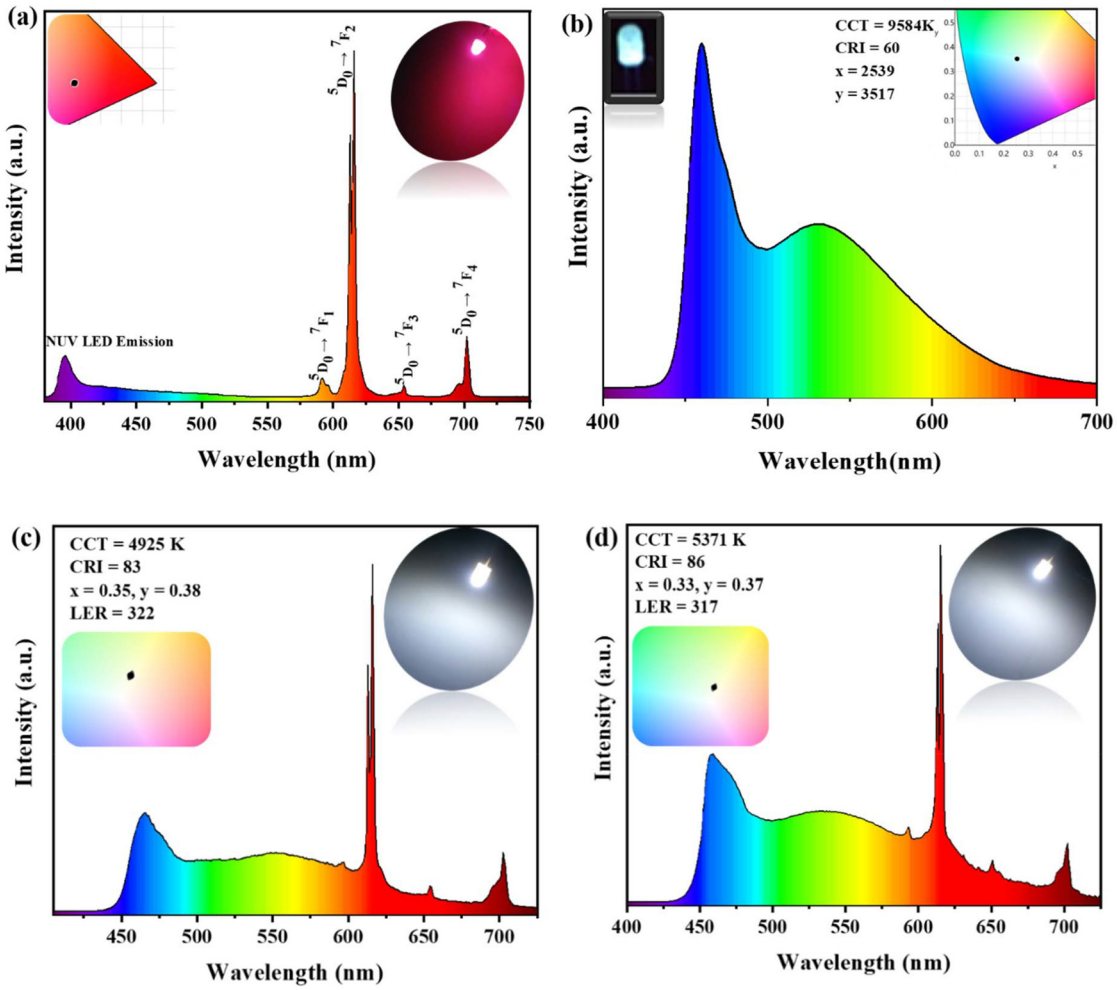

Fig. 12 EL spectrum of fabricated (a) red LED using NUV LED chip (b) white LED using a yellow organic dye and a blue LED chip. EL spectrum of fabricated white LEDs using a blue LED chip and yellow dye with (c) LLM:1.8Eu^{3+} and (d) solid solution phosphors.

estimated since the $^5D_0 \rightarrow {}^7F_6$ transition is not detectable in the system, which is beyond the visible range. The calculated *J–O* parameters are listed in Table ST8† for 395 nm excitation, while those for the CT band and 465 nm excitation are listed in Tables ST9 and ST10,† respectively. The calculated values showed that Ω_2 is much higher than Ω_4, indicating the dominance of ED transition in the emission spectra. This further supports the enhancement of red emission. The Ω_2 parameter demonstrates its dependence on the covalency between the RE cation and ligand field anions, providing insight into the Eu^{3+} site's surroundings and asymmetry. A higher degree of asymmetry was exhibited by the Eu^{3+} ions in the present host lattice, confirmed by the higher value of Ω_2. Variations in Ω_2 values were observed due to distortions around the Eu^{3+} ion site in the host lattice.

Fabrication of red and white LEDs

To assess the practical viability of the synthesized red phosphors for use in solid-state lighting (SSL), a red LED was fabricated by applying the LLM:1.8Eu^{3+} red phosphor onto the surface of a NUV LED chip and its electroluminescence (EL) spectra were recorded, as portrayed in Fig. 12. The EL spectrum includes many distinct emission bands between the wavelength region of 575–725 nm corresponding to the prominent emissions of Eu^{3+}, as well as a peak origination from the NUV LED located at 395 nm. A bright red emission was shown by the fabricated LED that is visible to the naked eye at a forward biased current of 20 mA (Fig. 12a), indicating the viability of the currently studied red phosphor for WLEDs. Moreover, it is essential to highlight that the red LED's spectral lines match the absorption spectra of phytochrome P_R (covers the blue and red spectral regions), as shown in Fig. S8.† To further confirm the usability of the produced compounds for indoor illumination, WLEDs were fabricated by combining the synthesized red phosphors with yellow organic dye[71] over the blue LED chip. Fig. 12c and d depict the EL spectrum of the fabricated WLED that is being powered using a 20 mA forward-biased current. The fabricated WLED exhibited superior white light with a good CRI and lower CCT of 83 and 4925 K, respectively. The inset of Fig. 12c shows the CIE color coordinate diagram of the emitted white light with coordinates of (x = 0.35, y = 0.38). In addition, the white LED's luminous efficiency of radiation (LER), which measures brightness as perceived by the unaided human eye in lumens per watt (lm W^{-1}), was evaluated, and the resulting value was approximately 322 lm W^{-1}. Nevertheless, the CRI value was enhanced to 86 with CCT = 5371 K and LER = 317 lm W^{-1} when the WLED was fabricated using the solid solution phosphor. To emphasize the importance of the red phosphor in WLED preparation, WLED was fabricated by taking only yellow

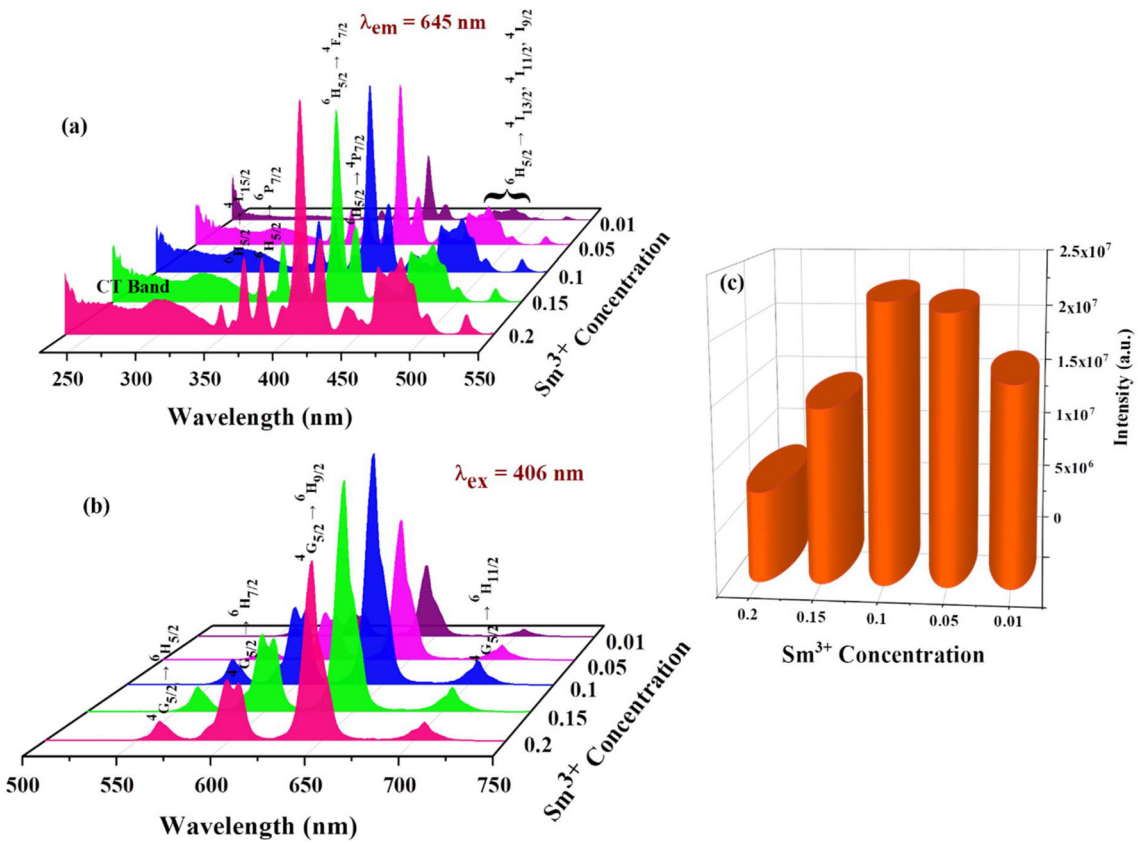

Fig. 13 PL (a) excitation and (b) emission spectra of LLM:$x$$Sm^{3+}$ phosphors (x = 0.01–0.2). (c) Bar diagram representation of the emission intensity of Sm^{3+} ions at 645 nm.

dye over a blue LED chip and observed a low CRI (60) and high CCT (9584 K) value (Fig. 12b). These critical results showed that the currently investigated red phosphor can be utilized in warm WLEDs.

Plant growth study

As red phosphors have significant applicability in indoor plant cultivation, Eu^{3+}-based red phosphors have recently received much attention as potential tools.[27,28,72] However, they are unable to cover the whole absorption spectrum of phytochrome P_R (Fig. S8†) because of the appearance of one major absorption band at 655 nm. As we know, the Sm^{3+} ion has its intense emission peak at 645 nm, so, to fulfil the requirement, co-doped $Li_2La_4(MoO_4)_7$:Sm^{3+},Eu^{3+} phosphors were synthesized and their PL properties were examined. In this context, an attempt has been made to investigate the PL properties of Sm^{3+}-activated $Li_2La_4(MoO_4)_7$ phosphors.

Fig. 13a and b depict the PLE and PL spectra of $Li_2La_4(MoO_4)_7$:Sm^{3+} phosphors. The excitation spectrum was recorded by monitoring the characteristic emission peak at 645 nm, which consisted of a broad band and several narrow peaks. The former was attributed to charge transfer transitions from O^{2-} to Sm^{3+} and Mo^{6+} ions, while the latter resulted from the 4f–4f electronic transitions of Sm^{3+} ions. Among all the transitions, the dominant excitation peak was observed at 405 nm due to the $^6H_{5/2} \rightarrow {}^4F_{7/2}$ transition, demonstrating that a commercial NUV LED chip could power the samples. The emission spectrum (λ_{ex} = 405 nm) consisted of four emission peaks (Fig. 13b) at approximately 580, 604, 645, and 704 nm owing to the $^4G_{5/2} \rightarrow {}^6H_{5/2}$, $^6H_{7/2}$, $^6H_{9/2}$, and $^6H_{11/2}$ transitions, respectively. The most intense peak was observed at 645 nm, which overlaps with the deep red region of the phytochrome P_R absorption, thus giving special attention to plant development.

A concentration-dependent PL study was carried out, and concentration quenching was observed at x = 0.1 (Fig. 13c). As previously mentioned, the simultaneous activation of Sm^{3+} and Eu^{3+} ions was implemented in the LLM host lattice to achieve complete coverage of the absorption spectrum of phytochrome P_R. To do so, the Sm^{3+} concentration was fixed at x = 0.1, and the concentration of Eu^{3+} ions varied from y = 0.02 to 0.12. Powder XRD patterns of the synthesized Sm^{3+} and Eu^{3+} co-doped phosphors are presented in Fig. S6.† The excitation and emission spectra of $Li_2La_{3.9-y}(MoO_4)_7$:0.1Sm^{3+},yEu^{3+} phosphors are portrayed in Fig. 14a and b. Analogous PLE spectra (a monitoring wavelength of 645 nm) were observed for the co-

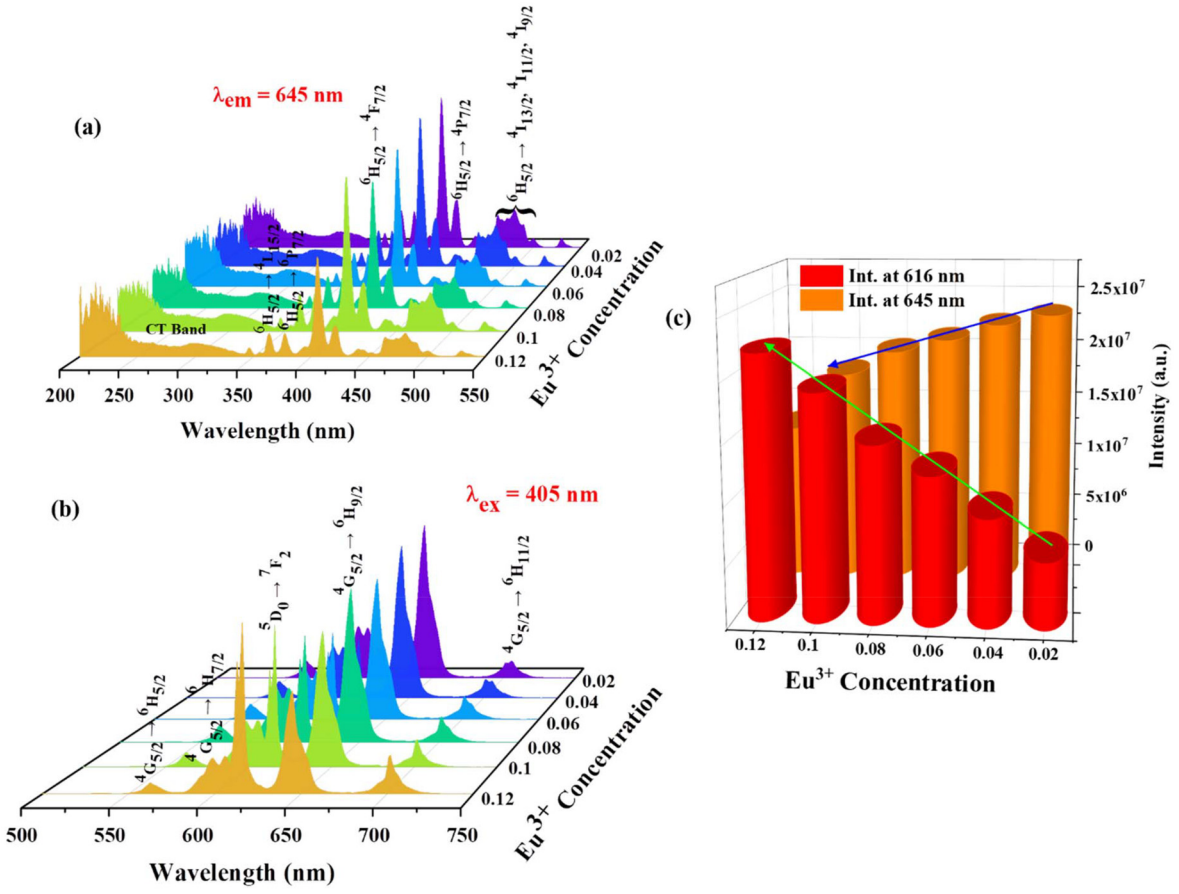

Fig. 14 PL (a) excitation and (b) emission spectra of LLM:0.1Sm^{3+},yEu^{3+} co-doped phosphors. (c) Bar diagram representation of changes in emission intensity at 616 nm (Eu^{3+}) and 645 nm (Sm^{3+}).

doped phosphors and the Sm^{3+} activated parent phosphor; nevertheless, their emission spectra were quite different. In the emission spectra (λ_{ex} = 405 nm), two major peaks were observed at 616 and 645 nm, corresponding to the $^5D_0 \rightarrow {}^7F_2$ and $^4G_{5/2} \rightarrow {}^6H_{9/2}$ transitions of Eu^{3+} and Sm^{3+}, respectively. With an increase in Eu^{3+} ion concentration, the emission intensity of the $^4G_{5/2} \rightarrow {}^6H_{9/2}$ decreased, while that of the $^5D_0 \rightarrow {}^7F_2$ transition increased as a result of energy transfer from Sm^{3+} to Eu^{3+} ions. The schematic representation of the energy transfer mechanism between the host lattice and both metal ions (Sm^{3+} and Eu^{3+}) is depicted in Fig. 15. Upon excitation at 405 nm, the host lattice and the RE metal ions (Sm^{3+} and Eu^{3+}) absorb photon energy and are promoted to their higher excited states. A portion of the excited electrons from the MoO_4^{2-} unit undergoes relaxation by returning to the ground level non-radiatively or transferring its energy to the excited states of Sm^{3+} and Eu^{3+} ions.

Additionally, under 405 nm excitation, Sm^{3+} ions excited from their ground level ($^6H_{5/2}$) to a higher excited state ($^4F_{7/2}$) and then relaxed to the lower excited level $^4G_{5/2}$ via non-radiative relaxation. Afterward, the electrons returned to the $^6H_{5/2}$, $^6H_{7/2}$, and $^6H_{9/2}$ energy levels radiatively and exhibiting corresponding emission peaks at 565, 604, and 645 nm, respectively. Meanwhile, the $^4G_{5/2}$ level of Sm^{3+} is comparable to the $^5D_0$ state of the Eu^{3+} ion. Nonetheless, we can confirm that the energy transfer direction is from Sm^{3+} ions to Eu^{3+} ions due to the higher energy of the $^4G_{5/2}$ level of Sm^{3+} compared to the $^5D_0$ level of Eu^{3+}. Moreover, the probability of phonon emission in the Sm^{3+} ($^4G_{5/2}$) → Eu^{3+} ($^5D_0$) process is more remarkable in contrast to capturing phonons for the Eu^{3+} ($^5D_0$) → Sm^{3+} ($^4G_{5/2}$) process.[73] Finally, all electrons in the lower excited state ($^5D_0$) return to the ground levels by emitting radiation, leading to the observation of the cross-relaxation phenomenon. Gradually, the emission intensity of the characteristic Sm^{3+} peaks decreased with increasing Eu^{3+} ion concentration due to effective energy transfer.

The lifetimes of Sm^{3+} with different concentrations of co-doped Eu^{3+} were examined to validate further the existence of energy transfer from Sm^{3+} to Eu^{3+}. The decay curves of LLM:0.1Sm^{3+},yEu^{3+} phosphors were recorded and are portrayed in Fig. 16a. All the samples showed similar types of decay curves and were well fitted by a bi-exponential function as the below equation:[74]

$$I(t) = I_0 + A_1 \exp\left(-\frac{t}{\tau_1}\right) + A_2 \exp\left(-\frac{t}{\tau_1}\right) \quad (13)$$

Here, the emission intensities of LLM:0.1Sm^{3+},yEu^{3+} phosphors were denoted as $I(t)$ and I_0 at time t and 0, respectively. A_1 and A_2 are the two fitting constants; τ_1 and τ_2 signify the fast and slow lifetimes in ms. Application of the following formula yielded the average lifetime (τ_{avg}) values:[75]

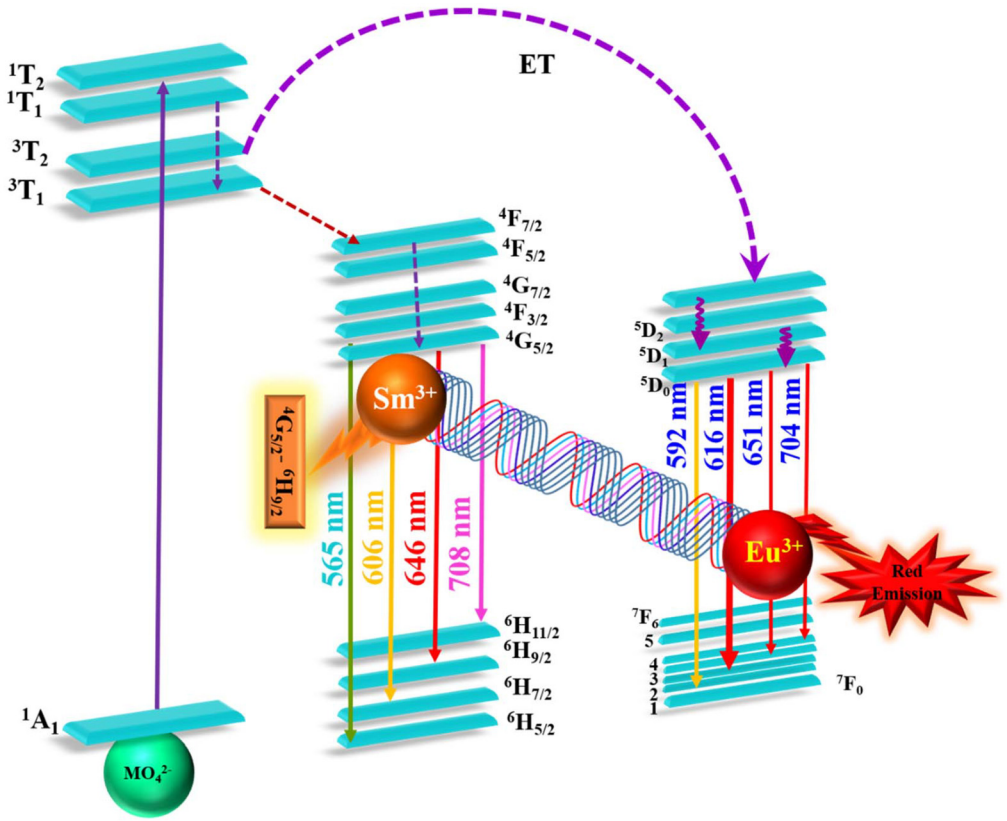

Fig. 15 Schematic representation of energy transfer process involved with the co-doped (Sm^{3+} and Eu^{3+}) phosphors.

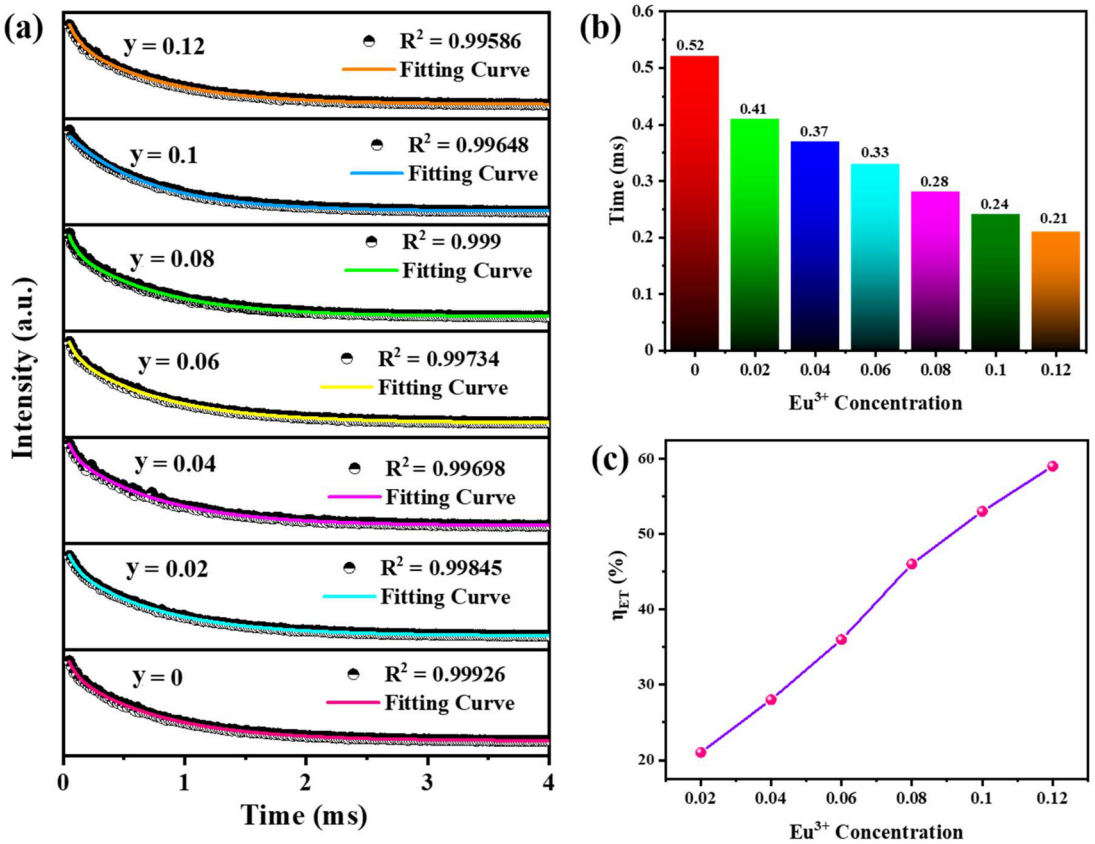

Fig. 16 (a) Lifetime decay curves of LLM:0.1Sm^{3+},yEu^{3+} co-doped phosphors (λ_{ex} = 405 nm). (b) Bar diagram representation of the calculated average lifetime values. (c) Energy transfer efficiency plot (from Sm^{3+} to Eu^{3+}).

$$\tau_{avg} = \frac{A_1\tau_1^2 + A_2\tau_2^2}{A_1\tau_1 + A_1\tau_2} \quad (14)$$

The τ_{avg} values were calculated, as presented in Fig. 16b, according to which the average lifetime values for co-doped phosphors were observed to decrease with an increase in the Eu^{3+} concentration, demonstrating the efficient charge transfer from Sm^{3+} to Eu^{3+} ions. Additionally, by using the following relationship, it is possible to determine the efficiency of energy transfer (η_{ET}) from Sm^{3+} to Eu^{3+}:[76]

$$\eta_{ET} = 1 - \frac{\tau_s}{\tau_{s_0}} \quad (15)$$

where τ_s and τ_{s_0} represent the lifetime of the sensitizer (Sm^{3+}) in the existence and exclusion of the activator (Eu^{3+}), respectively. As shown in Fig. 16c, the energy transfer efficiency increased monotonically upon increasing the concentration of Eu^{3+} ions in the LLM:0.1Sm^{3+} lattice. In this work, the highest ET efficiency was found to be 59.61%. In the lattice, the energy transfer from MoO_4^{2-} to Sm^{3+}/Eu^{3+} and Sm^{3+} to Eu^{3+} ions are graphically depicted in Fig. 15. Besides, the internal quantum efficiency (IQE) of $Li_2La_{3.78}(MoO_4)_7$:0.1Sm^{3+},0.1Eu^{3+} was measured and found to be 42.02% (Fig. S7†).

Ultimately, the optimal phosphor composition was determined by the comparable intensity of the metal ions Sm^{3+} ($^4G_{5/2} \rightarrow {}^6H_{9/2}$ transition) and Eu^{3+} ($^5D_0 \rightarrow {}^7F_2$ transition). The selected red phosphor ($Li_2La_{3.78}(MoO_4)_7$:0.1Sm^{3+},0.1Eu^{3+}) was coupled with a NUV LED chip to fabricate the deep red LED. Fig. 17 depicts the EL spectrum of the fabricated deep red LED, contrasted with the absorption spectrum of phytochrome P_R. The deep red LED EL spectrum precisely overlaps the phytochrome absorption spectrum. As can be seen from Fig. 17, two sorts of bands exhibited by phytochrome in the NUV and red region were covered by the NUV LED emission and red emission coming from the chosen phosphor $Li_2La_{3.78}(MoO_4)_7$:0.1Sm^{3+},0.1Eu^{3+}, respectively. This finding suggests the potential applicability of the $Li_2La_{3.78}(MoO_4)_7$:0.1Sm^{3+},0.1Eu^{3+} phosphor in plant growth studies.

Latent fingerprint (LFP) application

In forensic investigations, fingerprints are the most effective and convenient method for identifying specific people.[77,78] Fingerprints obtained at the crime scenes are latent; hence, an appropriate visualization technique was required to make them visible. The fingerprint powder dusting method is currently the most extensively used method for detecting latent fingerprints (LFPs).[4,79] Metal and magnetic powders are frequently utilized in this method, but they have numerous draw-

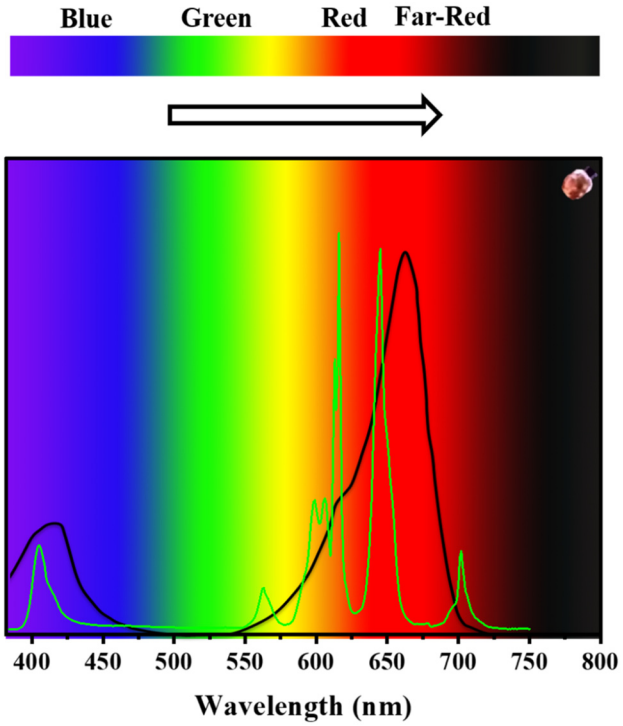

Fig. 17 Absorption spectrum of phytochrome P_R and the EL spectrum of the LLM:0.1Sm^{3+},0.1Eu^{3+} phosphor.

backs, including a poor display effect, expensive equipment, toxicity, unavoidable destruction, and difficulty operating.[79,80] Nowadays, fluorescent materials have attracted attention because of their good luminescence performance, ease of production, and minimal background interference. The exceptional physical and chemical properties of trivalent RE ion-doped inorganic compounds have attracted a lot of attention. Amid the RE ions, Eu^{3+} doped phosphors, when irradiated by UV light, form a narrow band that enables effective and delicate filtering of undesired backgrounds.[81] Currently, phosphors such as BaY_2ZnO_5:Eu^{3+},[82] $GdNb_2VO_9$:Eu^{3+},[83] and Ca_2InTaO_6:Eu^{3+} (ref. 84) have been reported for the generation of latent fingerprints. Fluorescent materials with little background interference and sharp contrast should be investigated to develop latent fingerprint visualization further.

To test the prepared phosphor's efficiency in latent fingerprint detection, fingerprint development was carried out on a glass surface using the LLM:1.8Eu^{3+} phosphor. For this, the hands of the donor were scrubbed clean with soap before being dried and afterward pressed smoothly over the surface of a glass slide. All fingerprints were collected from two male volunteers. The powdered phosphor samples were then spread over the surface of the already-formed fingerprint, and any extra powder was cleaned using a quill feather brush. Fig. 18 illustrates the image of the developed fingerprint under a UV lamp. Regardless of the substrate, the fingerprint pattern maintained high quality, and the fluorescent color stood out significantly from the backdrop interference. Under a UV lamp at 395 nm, the individual identity information contained in the fingerprint is still accessible using the LFP method. For personal identification, the macro and micro-level characteristics are crucial. Fingerprint features are categorized into three levels: level-I features (the overall fingerprint pattern), level-II features (local minutiae points), and level-III features (ridges and sweat pores). Fingerprint recognition makes use of both Level II and III features. Level-II characteristics are notably well-established and frequently utilized in fingerprint identification. However, level-III features offer more distinct individual information. As illustrated in Fig. 18, the whorl (1) and delta (2) are visible as level-I details. The eye, cross-over, bi-furcation, ridge ending, hook, and dot are clearly identified as level-II details. Level-III features play a crucial role in recognizing incomplete fingerprints. Sweat pores and incipient ridges are visible in this image as level-III details for personal identification.

To assess the potential of the currently investigated phosphor for LFPs on various surfaces, the LLM:1.8Eu^{3+} phosphor was applied on the surfaces of different objects, including glass, aluminum foil, and paper. Fig. 19 presents the developed fingerprints on the mentioned surfaces under daylight and UV lamps. As shown, the fingerprints are clearly visible when coated with the LLM:1.8Eu^{3+} phosphor, regardless of the material used. These results confirmed that the produced phosphors could be regarded as a promising fingerprint labeling agent in forensic science and individual identification.

Anti-counterfeiting application

Additionally, security ink (anti-counterfeiting) was a notable innovation used to guard against currency fraud and document forgeries. Significant economic harm has been caused by counterfeiting efforts for many years. Anti-counterfeiting techniques, including basic markers and security ink technologies, have been reported as ways to stop counterfeiting.[85–87] The transparent security ink solvent prevents personal document and money counterfeiting. However, traditional inks have some drawbacks, such as using hazardous solvents. A luminous, transparent ink solution with high contrast, high efficiency, non-toxicity, and selectivity is required to address these issues.[88,89] Amid numerous luminous materials, rare earth-doped ones have become promising materials owing to their remarkable optical properties. Recently, there have been few reports available on red emissive Eu^{3+} activated phosphors for anti-counterfeiting applications (SiO_2@$SrTiO_3$:Eu^{3+}, $CaGdSbWO_8$:Eu^{3+}, BaY_2ZnO_5:Eu^{3+}).[31,32,82]

Luminescent ink was prepared by adding polyvinyl alcohol (PVA) with distilled water in the proportion of 3 : 7 and thereafter heated at 90 °C with continuous stirring to get a transparent solution. A well-dispersed solution was obtained by adding LLM:Eu^{3+} to the initial solution and ultrasonically dispersing it for 30 minutes. Then, to verify their viability as anti-counterfeiting markings, marks were printed on black paper (with the National Institute of Technology Rourkela logo) and Indian currency. Fig. 20 illustrates the digital photographs of the anti-counterfeiting labels produced with the LLM:Eu^{3+} red phos-

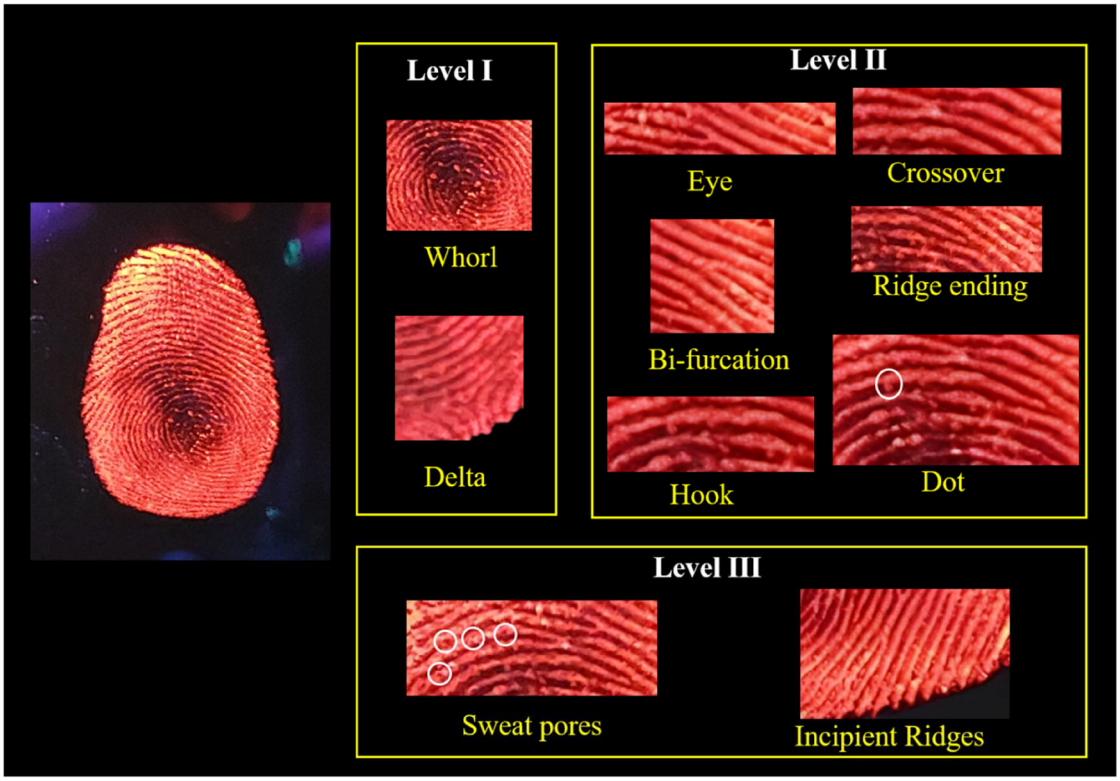

Fig. 18 Digital images of LFP by the LLM:1.8Eu^{3+} phosphor printed under UV lamp irradiation (levels I–III).

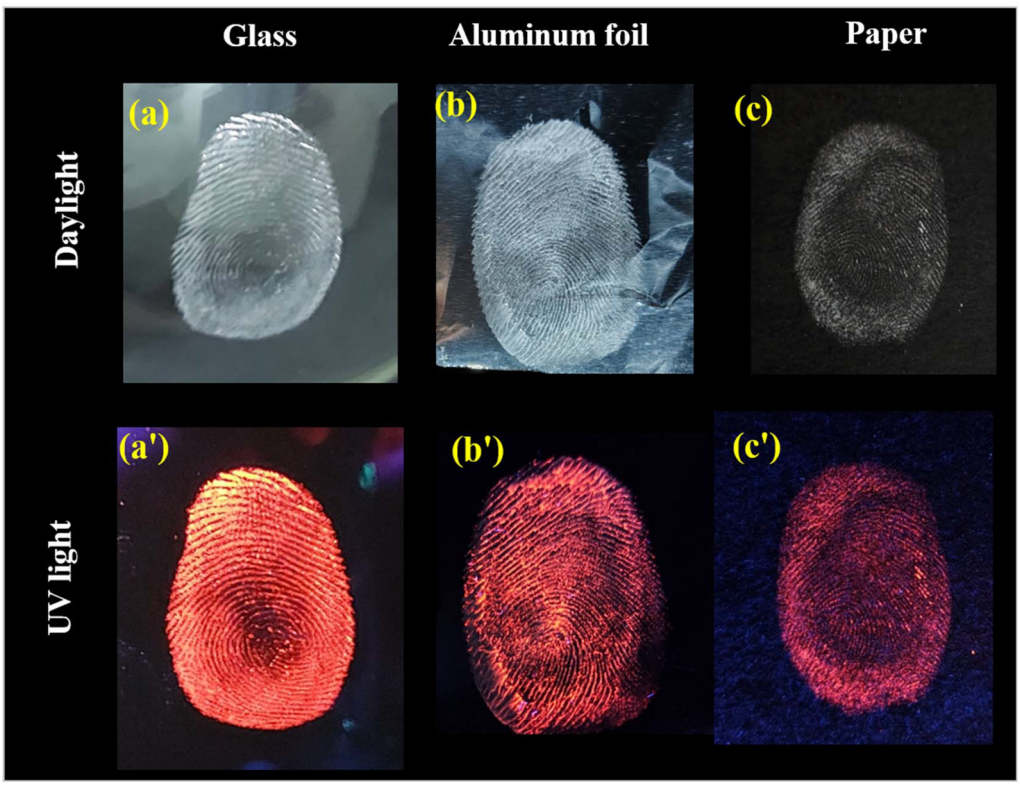

Fig. 19 Digital photographs of the developed LFPs with LLM:1.8Eu^{3+} on different surfaces under (a) daylight and (b) UV lamp.

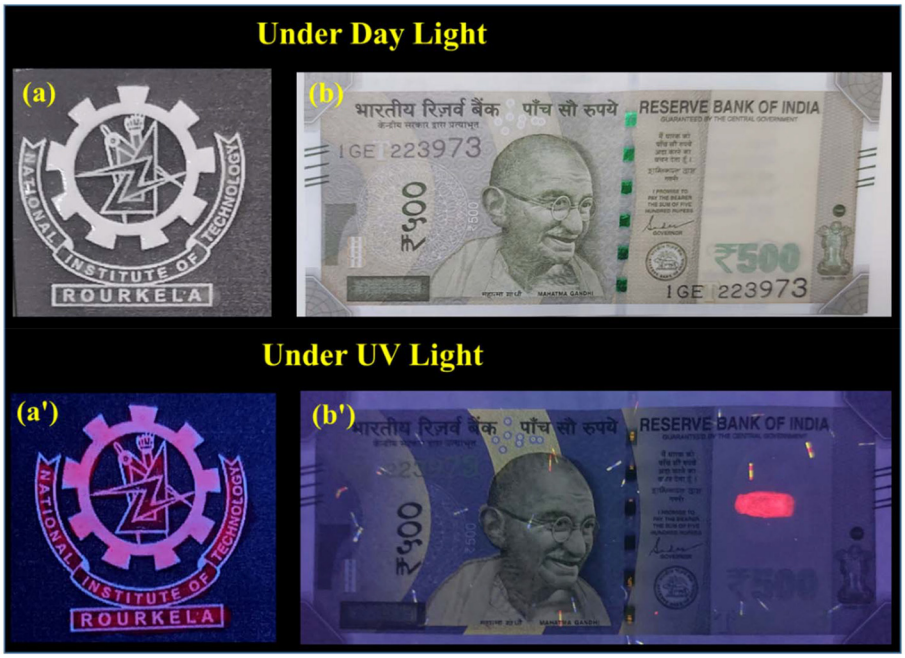

Fig. 20 Developed anti-counterfeit labels using the LLM:1.8Eu^{3+} phosphor under daylight (a, b) and UV light (a′, b′).

phor under daylight and 254/395 nm UV light. In contrast to what it appears to be to the human eye, the marks demonstrate substantial red emission with high contrast when exposed to NUV light. As a result, the LLM:Eu^{3+} security ink is anticipated to be used in information encryption and anti-counterfeiting cryptograms.

Conclusions

In conclusion, we have developed a series of LLM:Eu^{3+} narrow-band, efficient, red-emitting phosphors for versatile applications, synthesized *via* a high-temperature solid-state reaction. Under near-UV (395 nm) and blue (465 nm) light excitation, LLM:*x*Eu^{3+} phosphors exhibited bright red light emission at ~616 nm due to the $^5D_0 \rightarrow {}^7F_2$ (ED) transition of Eu^{3+} ions. The ideal doping concentration of Eu^{3+} ions in $Li_2La_4(MoO_4)_7$:*x*Eu^{3+} phosphors was x = 1.8, and exchange interaction is the prime concentration quenching mechanism. LLM:1.8Eu^{3+} showed good chromaticity coordinates (0.6697, 0.3299), quite close to the NTSC standard values, with a high color purity of 97.28%. The phosphor exhibited excellent thermal stability (81.75% at 150 °C) with good activation energy (E_a = 0.21), which was further enhanced to 86.12% in the case of the solid solution phosphor. The IQE of the LLM:1.8Eu^{3+} phosphor was found to be 89.6% and then increased as high as 92.54% for $Li_2La_{2.2}Eu_{1.8}(MoO_4)_4(WO_4)_3$. The fabricated white LED based on the LLM:1.8Eu^{3+} phosphor exhibited good color output with a high CRI (83) and low CCT (4925 K). However, employing the solid solution phosphor improved the CRI (86). The synthesized red phosphors also showed potential applications in the field of LFP and anti-counterfeiting. Additionally, a series of Sm^{3+}/Eu^{3+} co-doped phosphors were synthesized to create deep red LEDs for plant development (indoor plant cultivation). The red/deep-red LED was fabricated using the suitable LLM:0.1Sm^{3+},0.1Eu^{3+} co-doped phosphor, which precisely covered the absorption spectrum of photopigment phytochrome P_R. These outstanding results suggest the potential applicability of the currently synthesized phosphors in WLED, latent fingerprint, anti-counterfeiting, and plant growth study.

Data availability

The data supporting this article have been included as part of the ESI.†

Conflicts of interest

There are no conflicts to declare.

Acknowledgements

Some rights are reserved for the graphical abstract, figures and cover containing images of fingerprints. Permission must be sought by the consenting author/owner before being reproduced.

References

1 M.-H. Fang, Z. Bao, W.-T. Huang and R.-S. Liu, *Chem. Rev.*, 2022, **122**, 11474–11513.

2 A. J. Kenyon, *Prog. Quantum Electron.*, 2002, **26**, 225–284.
3 S. Fang, T. Lang, M. Cai and T. Han, *J. Alloys Compd.*, 2022, **902**, 163825.
4 M. Wang, M. Li, A. Yu, J. Wu and C. Mao, *ACS Appl. Mater. Interfaces*, 2015, **7**, 28110–28115.
5 P. Kumar, J. Dwivedi and B. K. Gupta, *J. Mater. Chem. C*, 2014, **2**, 10468–10475.
6 C. Bouzigues, T. Gacoin and A. Alexandrou, *ACS Nano*, 2011, **5**, 8488–8505.
7 P. Mahata, S. K. Mondal, D. K. Singha and P. Majee, *Dalton Trans.*, 2017, **46**, 301–328.
8 X. Huang, *Nat. Photonics*, 2014, **8**, 748–749.
9 G. Li, Y. Tian, Y. Zhao and J. Lin, *Chem. Soc. Rev.*, 2015, **44**, 8688–8713.
10 V. Bachmann, C. Ronda and A. Meijerink, *Chem. Mater.*, 2009, **21**, 2077–2084.
11 P. Pust, V. Weiler, C. Hecht, A. Tücks, A. S. Wochnik, A.-K. Henß, D. Wiechert, C. Scheu, P. J. Schmidt and W. Schnick, *Nat. Mater.*, 2014, **13**, 891–896.
12 S. Ye, F. Xiao, Y. X. Pan, Y. Y. Ma and Q. Y. Zhang, *Mater. Sci. Eng., R*, 2010, **71**, 1–34.
13 K. Uheda, N. Hirosaki, Y. Yamamoto, A. Naito, T. Nakajima and H. Yamamoto, *Electrochem. Solid-State Lett.*, 2006, **9**, H22.
14 V. Bachmann, C. Ronda, O. Oeckler, W. Schnick and A. Meijerink, *Chem. Mater.*, 2009, **21**, 316–325.
15 L. Wang, R.-J. Xie, T. Suehiro, T. Takeda and N. Hirosaki, *Chem. Rev.*, 2018, **118**, 1951–2009.
16 H. Zhu, C. C. Lin, W. Luo, S. Shu, Z. Liu, Y. Liu, J. Kong, E. Ma, Y. Cao and R.-S. Liu, *Nat. Commun.*, 2014, **5**, 1–10.
17 C. C. Lin, A. Meijerink and R.-S. Liu, *J. Phys. Chem. Lett.*, 2016, **7**, 495–503.
18 A. Volokitina, P. Loiko, E. Vilejshikova, X. Mateos, E. Dunina, A. Kornienko, N. Kuleshov and A. Pavlyuk, *J. Alloys Compd.*, 2018, **762**, 786–796.
19 N. Yeh and J.-P. Chung, *Renewable Sustainable Energy Rev.*, 2009, **13**, 2175–2180.
20 W. Xia, Y. Ye, Q. Mao, Y. Ding, X. Li, M. Liu and J. Zhong, *Mater. Today Chem.*, 2024, **36**, 101958.
21 L. Qin, S. Bi, P. Cai, C. Chen, J. Wang, S. Il Kim, Y. Huang and H. J. Seo, *J. Alloys Compd.*, 2018, **755**, 61–66.
22 Y. Zheng, H. Zhang, H. Zhang, Z. Xia, Y. Liu, M. S. Molokeev and B. Lei, *J. Mater. Chem. C*, 2018, **6**, 4217–4224.
23 Z. Zhou, J. Zheng, R. Shi, N. Zhang, J. Chen, R. Zhang, H. Suo, E. M. Goldys and C. Guo, *ACS Appl. Mater. Interfaces*, 2017, **9**, 6177–6185.
24 Q. Wu, P. Li, Z. Ye, X. Huo, H. Yang, Y. Wang, D. Wang, J. Zhao, Z. Yang and Z. Wang, *Inorg. Chem.*, 2021, **60**, 16593–16603.
25 Y. Ke, Y. Wang, Y. Liu, S. Chen, J. Luo, J. Wang, T. Wang, J. Zhao, B. Deng and R. Yu, *J. Alloys Compd.*, 2021, **851**, 156875.
26 M. T. Tran, D. Q. Trung, N. Tu, D. D. Anh, L. T. H. Thu, N. V. Du, N. V. Quang, N. T. Huyen, N. D. T. Kien and D. X. Viet, *J. Alloys Compd.*, 2021, **884**, 161077.
27 X. Li, J. Ding, Q. Zeng, X. Lin, L. Jiang and A. Wu, *Dalton Trans.*, 2024, **53**, 16929–16940.
28 S. Miao, R. Shi, Y. Zhang, D. Chen and Y. Liang, *Adv. Mater. Technol.*, 2023, **8**, 2202103.
29 F. Ding, Y. Zhou, Y. He, Y. Liang, P. Luo, W. Zhou, J. Zhang, L. Yu, Z. Qiu and S. Lian, *Inorg. Chem.*, 2023, **62**, 3141–3152.
30 P. Ling-Hu, X. Guo, J. Hu, C. Deng and R. Cui, *Adv. Opt. Mater.*, 2024, **12**, 2301760.
31 A. Sandhyarani, M. K. Kokila, G. P. Darshan, R. B. Basavaraj, B. D. Prasad, S. C. Sharma, T. K. S. Lakshmi and H. Nagabhushana, *Chem. Eng. J.*, 2017, **327**, 1135–1150.
32 W. Shi, J. Chen, J. Kong, Z. Ma, J. Gao, J. Guo, Z. Hu, Q. Lv, B. Deng and W. Chen, *J. Alloys Compd.*, 2022, **914**, 165134.
33 J. T. Ingle, A. B. Gawande, R. P. Sonekar, S. K. Omanwar, Y. Wang and L. Zhao, *J. Alloys Compd.*, 2014, **585**, 633–636.
34 A. Katelnikovas, J. Plewa, S. Sakirzanovas, D. Dutczak, D. Enseling, F. Baur, H. Winkler, A. Kareiva and T. Jüstel, *J. Mater. Chem.*, 2012, **22**, 22126–22134.
35 F. Esteban-Betegón, C. Zaldo and C. Cascales, *Chem. Mater.*, 2010, **22**, 2315–2324.
36 X. Huang, B. Li, P. Du, H. Guo, R. Cao, J. S. Yu, K. Wang and X. W. Sun, *Dyes Pigm.*, 2018, **151**, 202–210.
37 S. Vaidyanathan and D. Y. Jeon, *Int. J. Appl. Ceram. Technol.*, 2009, **6**, 453–458.
38 R. K. Pandey, *J. Phys. Soc. Jpn.*, 1974, **36**, 177–178.
39 F. Guo, R. Zhang, Z. Cui, C. Liu and J. Chen, *Opt. Mater.*, 2012, **35**, 227–230.
40 Z. Yu, Z. Luo, X. Liu, E. Y. B. Pun and H. Lin, *Opt. Mater.*, 2019, **93**, 76–84.
41 J. Ru, S. Ying, W. Zheng and J. Chen, *Mater. Res. Bull.*, 2016, **84**, 468–473.
42 B. Zhao, F. Chen, J. Ru, F. Guo and J. Chen, *ECS J. Solid State Sci. Technol.*, 2021, **10**, 56002.
43 M. Rajendran and S. Vaidyanathan, *J. Alloys Compd.*, 2019, **789**, 919–931.
44 M. Rajendran and S. Vaidyanathan, *New J. Chem.*, 2020, **44**, 14823–14836.
45 R. M. Hazen, L. W. Finger and J. W. E. Mariathasan, *J. Phys. Chem. Solids*, 1985, **46**, 253–263.
46 D. L. Shruthi, G. N. A. Kumar and A. J. Reddy, *Ceram. Int.*, 2021, **47**, 16342–16357.
47 N. M. Kozhevnikova and O. A. Kopylova, *Russ. J. Inorg. Chem.*, 2011, **56**, 935–938.
48 J. Yang, Y. Liang, K. Li, G. Yang, Y. Zhu, S. Liu and W. Lei, *Appl. Surf. Sci.*, 2018, **458**, 769–780.
49 D. L. Wood and J. S. Tauc, *Phys. Rev. B*, 1972, **5**, 3144.
50 P. K. Vishwakarma, S. B. Rai and A. Bahadur, *Mater. Res. Bull.*, 2021, **133**, 111041.
51 V. Chauhan, P. K. Pandey, P. Dixit, P. Deshmukh, S. Satapathy and P. C. Pandey, *J. Lumin.*, 2022, **248**, 118994.
52 N. Yang, J. Li, Z. Zhang, D. Wen, Q. Liang, J. Zhou, J. Yan and J. Shi, *Chem. Mater.*, 2020, **32**, 6958–6967.

53 A. Bindhu, J. I. Naseemabeevi and S. Ganesanpotti, *Adv. Photonics Res.*, 2022, **3**, 2100159.
54 P. Du, W. Ran, Y. Hou, L. Luo and W. Li, *ACS Appl. Nano Mater.*, 2019, **2**, 4275–4285.
55 B. R. Judd, *Phys. Rev.*, 1962, **127**, 750.
56 L. Li, W. Chang, J. He, Y. Yan, M. Cui, S. Jiang, G. Xiang and X. Zhou, *J. Alloys Compd.*, 2018, **763**, 278–288.
57 G. Blasse, *Philips Res. Rep.*, 1969, **24**, 131.
58 S. Huang and L. Lou, *Chin. J. Lumin.*, 1990, **11**, 1.
59 K. Li, M. Shang, H. Lian and J. Lin, *J. Mater. Chem. C*, 2016, **4**, 5507–5530.
60 J. Grigorjevaite and A. Katelnikovas, *ACS Appl. Mater. Interfaces*, 2016, **8**, 31772–31782.
61 X. Huang, H. Guo, J. Liang and S. Wang, *Inorg. Chem. Commun.*, 2020, **116**, 107938.
62 M. Song, L. Wang, Y. Feng, H. Wang, X. Wang and D. Li, *Opt. Mater.*, 2018, **84**, 284–291.
63 X. Huang, H. Guo and B. Li, *J. Alloys Compd.*, 2017, **720**, 29–38.
64 Y. Li, Y. Yin, T. Wang, J. Wu, J. Zhang, S. Yu, M. Zhang, L. Zhao and W. Wang, *Dalton Trans.*, 2021, **50**, 4159–4166.
65 Y. Guo, S. H. Park, B. C. Choi, J. H. Jeong and J. H. Kim, *Sci. Rep.*, 2017, **7**, 15884.
66 L. Li, W. Chang, W. Chen, Z. Feng, C. Zhao, P. Jiang, Y. Wang, X. Zhou and A. Suchocki, *Ceram. Int.*, 2017, **43**, 2720–2729.
67 Q. Liu, L. Wang, W. Huang, X. Li, M. Yu and Q. Zhang, *Ceram. Int.*, 2018, **44**, 1662–1667.
68 R. B. Lauer, *J. Phys. Chem. Solids*, 1973, **34**, 249–253.
69 G.-H. Li, N. Yang, J.-G. Guo, Z.-L. Wang, G.-M. Cai and X.-J. Wang, *Dalton Trans.*, 2020, **49**, 3260–3271.
70 E. Cantelar, J. A. Sanz-García, A. Sanz-Martin, J. E. M. Santiuste and F. Cussó, *J. Alloys Compd.*, 2020, **813**, 152194.
71 A. B. Kajjam, S. Giri and S. Vaidyanathan, *Mater. Chem. Front.*, 2017, **1**, 512–520.
72 P. Ling-Hu, X. Guo, J. Hu, C. Deng and R. Cui, *Adv. Opt. Mater.*, 2024, **12**, 2301760.
73 D. Huang, Y. Zhou, W. Xu, Z. Yang, Z. Liu, M. Hong, Y. Lin and J. Yu, *J. Alloys Compd.*, 2013, **554**, 312–318.
74 C.-T. Chen, T.-J. Lin, M. S. Molokeev and W.-R. Liu, *Dyes Pigm.*, 2018, **150**, 121–129.
75 J. Zhong, M. Xu, D. Chen, G. Xiao and Z. Ji, *Dyes Pigm.*, 2017, **146**, 272–278.
76 X. Min, Z. Huang, M. Fang, Y.-G. Liu, C. Tang and X. Wu, *Inorg. Chem.*, 2014, **53**, 6060–6065.
77 S. Yang, C. Wang and S. Chen, *Angew. Chem., Int. Ed.*, 2011, **16**, 3790–3793.
78 K. Song, P. Huang, C. Yi, B. Ning, S. Hu, L. Nie, X. Chen and Z. Nie, *ACS Nano*, 2015, **9**, 12344–12348.
79 G. S. Sodhi and J. Kaur, *Forensic Sci. Int.*, 2001, **120**, 172–176.
80 J. Shao, J. Yan, X. Li, S. Li and T. Hu, *Dyes Pigm.*, 2019, **160**, 555–562.
81 D. Navami, R. B. Basavaraj, S. C. Sharma, B. Daruka Prasad and H. Nagabhushana, *J. Alloys Compd.*, 2018, **762**, 763–779.
82 G. Rajkumar, V. Ponnusamy, G. V. Kanmani and M. T. Jose, *Ceram. Int.*, 2022, **48**, 10–21.
83 Y. Li, J. Kong, C. Li, H. Su, Y. Du, L. Zhou, Z. Zou, B. Deng, X. Ji and R. Yu, *J. Alloys Compd.*, 2023, **940**, 168716.
84 X. Ouyang, R. Liu, X. Hu, J. Li, R. Tang, X. Jin, S. Chen, X. Yao, B. Deng and H. Geng, *J. Alloys Compd.*, 2023, **939**, 168715.
85 W. Ren, G. Lin, C. Clarke, J. Zhou and D. Jin, *Adv. Mater.*, 2020, **32**, 1901430.
86 V. K. Singh, R. K. Chitumalla, S. K. Ravi, Y. Zhang, Y. Xi, V. Sanjairaj, C. Zhang, J. Jang and S. C. Tan, *ACS Appl. Mater. Interfaces*, 2017, **9**, 33071–33079.
87 P. Pei, R. Wei, B. Wang, J. Su, Z. Zhang and W. Liu, *Adv. Funct. Mater.*, 2021, **31**, 2102479.
88 H. Liu, W. Zhang, H. Liang, Q. Zeng, J. Shi and D. Wen, *J. Mater. Chem. C*, 2021, **9**, 1622–1631.
89 K. N. Narasimhamurthy, G. P. Darshan, S. C. Sharma, H. B. Premkumar, H. Adarsha and H. Nagabhushana, *J. Colloid Interface Sci.*, 2021, **600**, 887–897.

